A high resolution spectral element approximation of viscoelastic flows in axisymmetric geometries using a DEVSS-G/DG formulation☆

R.M. Kynch, T.N. Phillips*

School of Mathematics, Cardiff University, Senghennydd Road, Cardiff CF24 4AG, United Kingdom

ABSTRACT

The discretisation of benchmark viscoelastic flow problems in axisymmetric geometries using the spectral element method is considered. The computations are stabilized using the DEVSS-G/DG formulation of the governing equations. A decoupled approach is employed in which the conservation equations are solved for velocity and pressure and the constitutive equation (Oldroyd-B and Giesekus) are solved for the polymeric component of the extra-stress tensor. The method is validated for the start-up of transient Poiseuille flow for which an analytical solution exists. A comprehensive set of results is presented for flow past a fixed sphere for the Oldroyd B and Giesekus models. Excellent agreement is found with results in the literature on the drag experienced by the sphere. Evidence is provided which shows the existence of a limiting Weissenberg number due to the inability to resolve the high gradients in axial stress in the wake of the sphere through polynomial enrichment. The shear-thinning property of the Giesekus model leads to a reduction in drag compared to the Oldroyd B model at equivalent values of the Weissenberg number and viscosity ratio. The numerical simulations eventually fail to converge for the Giesekus model which suggests that factors other than solely extensional properties are responsible for this behaviour. The influence of the Reynolds number and, for the Giesekus model, the mobility parameter on the drag coefficient is also investigated and discussed.

1. Introduction

The computational simulation of flows involving viscoelastic fluids is a challenging task. The challenges present themselves in the choices of both the constitutive model for the fluid, and the numerical method used to approximate the solution in the chosen geometry. The choice of model must be made carefully, depending on the properties of the fluid and the dynamics of the flow which one wishes to simulate. The selected numerical method must be robust in terms of stability and accuracy. Few analytical solutions are available to validate the numerical method so it has become standard to use benchmark problems as a means of understanding the chosen model and validating the numerical scheme employed.

One established transient benchmark problem is that of a sphere of radius R_S falling at constant speed V_S inside a cylindrical tube [1]. This problem is one of the oldest problems in the study of fluid dynamics. It dates back to the work of Stokes in the mid 1800s [2] and has received continuing attention in the subsequent literature: a thorough history of the benchmark in the classical sense can be found in [3]. It is common to consider the problem in the frame of reference of the sphere and the walls, in the framework of the sphere, move upwards with uniform speed V_S and therefore in the opposite direction to the gravitational force.

In the context of viscoelastic flows, despite the simplistic nature of the geometry, this benchmark problem continues to present a challenging test for numerical schemes. The complex combination of shear and extensional flow regions and increasingly thin boundary layers has made consistent experimental and numerical results difficult to obtain [4]. The benchmark problem is also of practical interest in the context of flow around obstacles, for example in sedimentation, the settling of suspensions, rheometry and in industrial settings where particles are present (such as mineral and chemical processing or combustion engines).

It has become common that comparisons for this benchmark are made for the particular configuration in which the ratio of tube-to-sphere radius is 2 : 1 using the drag force, D computed on the surface of the sphere when the flow has reached a steady state. It is typical to make comparisons using the value of the

drag factor

$$D^* = \frac{D}{6\pi \eta_0 R_S V_S} \tag{1}$$

normalised using the drag experienced by the sphere in an unbounded expanse of Newtonian fluid with viscosity η_0. However, it has generally been agreed that, while useful, the drag factor does not provide enough insight into the global accuracy of the solution found by a numerical method [4,5], particularly as certain components of the stress do not feature in the calculation. It is therefore wise to provide further insight into the quality of the solution obtained using quantities such as the velocity and stress.

There are numerical results available for many models in the literature, with the upper-convected Maxwell (UCM) model featuring heavily in the literature (for example, Rasmussen and Hassager [6], Crochet and Legat [7], Baaijens et al. [8]). Other constitutive models considered include Oldroyd B, FENE-type, PTT and Giesekus [4]. The present work is focused on the Oldroyd B and Giesekus models.

Among the studies published on this benchmark using the Oldroyd B model (for example, see Lunsmann et al. [9], Bodart and Crochet [10], Tamaddon-Jahromi et al. [11]), only a few have used high-order methods (such as spectral or hp-finite element methods with high p), with most methods relying instead on very fine meshes (resulting in relatively high numbers of degrees of freedom) in order to show mesh convergence. Examples of higher-order methods applied to the problem are the spectral p-adaptive strategy of Chauvière and Owens [5] and the hp-adaptive finite element method of Fan [12] who together find agreement in the limiting Weissenberg number for this model. As with the UCM model there is a set of results which allows one to compile comprehensive tables of drag factors for comparison by other authors.

In the case of the Giesekus model, there have been many studies involving spheres, particularly in the investigation of experimentally observed phenomena (for example, Baaijens et al. [8], Yang and Khomami [13], Harlen [14]). However, there exist no definitive benchmark results available in the literature for the Giesekus model, at least in the sense that they are available for UCM and Oldroyd B models.

The aim of this paper is to apply a high-resolution spectral element method to the problem of benchmark of uniform flow past a fixed sphere for the Oldroyd B and Giesekus constitutive models, with model parameters commonly used by other authors. Our spectral element method is applied to a DEVSS-G/DG formulation of the problem to provide stabilisation. We shall present results which are convergent with respect to the spectral polynomial order, p, using a minimal number of elements. These results will add to those available in the literature for the Oldroyd B model and provide a reference for the Giesekus model, where few comprehensive results for this benchmark are available. A similar method, with a different implementation, has been successfully applied to the benchmark of flow past a cylinder [15] for these constitutive models and this paper will extend the available results with these techniques to the sphere benchmark problem.

This paper is arranged as follows. In Section 2 we describe the formulation of the governing equations including the DEVSS-G stabilisation and an alternative treatment of the continuity equation and also provide a brief discussion of the rheological behaviour of the constitutive models considered. In Section 3 we state the formulation of the sphere benchmark problem and how boundary conditions will be applied. Section 4 details the numerical methods applied to the temporal and spatial discretisations of the governing equations and how this is handled computationally. In Section 5 we present verification of our numerical scheme using the analytical solution for transient start-up of Poiseuille flow of an Oldroyd B fluid. This is followed by results for the sphere

benchmark for the Oldroyd B and Giesekus models. Finally, in Section 6 we provide some concluding remarks.

2. Governing equations

Consider the Navier-Stokes equations in dimensionless form

$$Re\frac{D\mathbf{u}}{Dt} = -\nabla p + \beta\nabla^2\mathbf{u} + \nabla\cdot\boldsymbol{\tau} + \mathbf{f}, \tag{2}$$

$$\nabla\cdot\mathbf{u} = -\mu\int_\Omega p\,d\Omega, \tag{3}$$

where the field variables are velocity, $\mathbf{u}$, pressure, p, and elastic stress, $\boldsymbol{\tau}$, and $\mu > 0$ is a constant. The dimensionless groups are the Reynolds number, Re, and the viscosity ratio, β, which is the ratio of solvent to total viscosity.

The alternative statement of the continuity Eq. (3), proposed by Gwynllyw and Phillips [16] is a means of removing the indeterminacy in the pressure. It also ensures that when the weak statement of the problem is discretized, the pressure approximation is consistent with the choice of solution space, which requires that pressure possesses vanishing mean. There are also benefits to be gained in terms of the conditioning of the discrete problem albeit at the expense of a loss of sparsity in the global discrete system.

The system is closed by a constitutive law relating the elastic stress to the rate-of-deformation tensor, $\mathbf{d} = \frac{1}{2}(\nabla\mathbf{u} + \nabla\mathbf{u}^T)$. We consider the Giesekus [17] constitutive model for a viscoelastic fluid

$$\boldsymbol{\tau} + We\left(\overset{\triangledown}{\boldsymbol{\tau}} + \frac{\alpha}{(1-\beta)}\boldsymbol{\tau}^2\right) = 2(1-\beta)\mathbf{d} \tag{4}$$

where the dimensionless group We is the Weissenberg number and $\alpha > 0$ is the mobility parameter. We note that the Oldroyd B model [18] is a special case of (4) with $\alpha = 0$. We define the upper-convected derivative of a general tensor field, $\mathbf{G}$, by

$$\overset{\triangledown}{\mathbf{G}} = \frac{\partial\mathbf{G}}{\partial t} + \mathbf{u}\cdot\nabla\mathbf{G} - \mathbf{G}\cdot\nabla\mathbf{u} - (\nabla\mathbf{u})^T\cdot\mathbf{G}. \tag{5}$$

2.1. Model properties

The rheological properties of the constitutive models considered play an important role in terms of the type of behaviour that may be investigated using them. Two simple flows which provide insight into the model behaviour are uniaxial extension and simple shear, both of which are important mechanisms in flows involving spheres, with shear occurring near the surface of the sphere and extension occurring in the wake.

The Oldroyd model predicts an infinite extensional viscosity at a finite shear-rate (namely at $\dot\epsilon = \frac{1}{2We}$). This is an undesirable and unphysical property particularly when modelling flows involving extension. The Giesekus model does not suffer from this problem and predicts finite values at all extension rates with a limiting value [19] of $3\beta + 2\frac{(1-\beta)}{\alpha}$ for large extension rates. The Oldroyd B model predicts a constant shear viscosity whereas the Giesekus model predicts shear-thinning, with the rate of thinning with shear-rate increasing with the mobility parameter. The limiting behaviour of the Giesekus model is independent of the mobility parameter and tends to the solvent viscosity, i.e. β, for large shear-rates. The Oldroyd B model predicts a quadratic relationship between the first normal stress difference and shear-rate and a zero second normal stress difference. At low shear-rates the Giesekus model predicts a quadratic relationship between the first normal stress difference and shear-rate. However, this becomes linear at large shear-rates. The Giesekus model predicts a non-zero second normal stress difference, which tends to the value $-\frac{(1-\beta)}{We}$ with increasing shear-rate.

2.2. DEVSS-G

The governing equations are written in a modified but mathematically equivalent form to stabilise the corresponding discretisation. A version of the DEVSS-G [20] method, proposed by Bogaerds et al. [21], is employed. In this formulation the components of the velocity gradient tensor are introduced as additional variables. An L^2-projection of the velocity gradient, denoted by $\mathbf{G}$, is introduced as an additional variable in the system of equations in order to increase the elliptic nature of the equations as follows

$$Re\frac{D\mathbf{u}}{Dt} - (\beta + \theta)\nabla^2\mathbf{u} + \theta\nabla\cdot\mathbf{G} + \nabla p = \nabla\cdot\boldsymbol{\tau}, \tag{6}$$

$$\nabla\cdot\mathbf{u} + \mu\int_\Omega pd\Omega = 0, \tag{7}$$

$$\mathbf{G} - \nabla\mathbf{u} = 0. \tag{8}$$

where θ is the DEVSS-G stabilisation parameter, typically chosen to be equal to $(1-\beta)$ to make the coefficient of $\nabla^2\mathbf{u}$ unity.

This is an alternative to the original DEVSS-G formulation proposed by Liu et al. [20] in that the stabilising term in the momentum equation is the velocity gradient, rather than the rate-of-strain tensor, $\mathbf{G} + \mathbf{G}^T$. The reasoning for this choice is that the method of Bogaerds et al. [21] complements our enforcement of $\nabla\cdot\mathbf{u}^T = 0$ in the momentum Eq. (2) due to incompressibility. If this constraint was not enforced, the Laplacian in (2) would be replaced by $\nabla\cdot(\nabla\mathbf{u} + \nabla\mathbf{u}^T)$ and so the stabilisation by the rate-of-strain tensor appears to be more natural.

3. Formulation of problem

We now consider the initial and boundary conditions required to solve this problem. For all cases considered, zero initial conditions are applied on velocity and stress.

We decompose the boundary into distinct sections

$$\Gamma = \Gamma^- \cup \Gamma^+ \cup \Gamma^W \cup \Gamma^C \cup \Gamma^S \tag{9}$$

where Γ^- and Γ^+ are inflow and outflow boundaries, Γ^W and Γ^C are wall and sphere wall boundaries and Γ^S is the axis of symmetry.

We prescribe velocity at inflow and outflow, apply no-slip conditions on walls and axisymmetric boundary conditions along the axis of symmetry

$$\mathbf{u} = \mathbf{u}_{in} \text{ on } \Gamma^-, \tag{10}$$

$$\mathbf{u} = \mathbf{u}_{out} \text{ on } \Gamma^+, \tag{11}$$

$$\mathbf{u} = \mathbf{0} \text{ on } \Gamma^W, \tag{12}$$

$$\mathbf{u} = \mathbf{0} \text{ on } \Gamma^C, \tag{13}$$

$$\mathbf{u} \cdot \mathbf{n} = \mathbf{0} \text{ on } \Gamma^S. \tag{14}$$

where $\mathbf{u}_{in}$ and $\mathbf{u}_{out}$ are known and are chosen according to the geometry and problem of interest. In the case of a moving wall, as in the case of flow past a sphere, we set $\mathbf{u}_{in} = \mathbf{u}_{out}$ and $\mathbf{u} = \mathbf{u}_{in}$ on Γ^W.

Further, we must prescribe a boundary condition on the elastic stress at inflow

$$\boldsymbol{\tau} = \boldsymbol{\tau}_{in} \text{ on } \Gamma^-, \tag{15}$$

where $\boldsymbol{\tau}_{in}$ is typically found by substituting the known velocity solution into the constitutive equation and solving for $\boldsymbol{\tau}$. This is fairly trivial for the majority of boundary conditions we shall be considering. There are solutions available for a limited range of complicated boundary conditions, such as transient pipeflow.

4. Numerical discretisation

The system of equations is solved in both space and time and therefore a discretisation of each is required. The following section details the numerical methods and approximations used to achieve this.

4.1. Temporal discretisation

Consider a uniform discretisation in time with timestep Δt so that $t^n = n\Delta t$ is the nth timestep. Let $\mathbf{f}^n = \mathbf{f}(\mathbf{x}, t^n)$ denote the evaluation of a function, $\mathbf{f}(\mathbf{x}, t)$, at timestep n. We decouple the velocity-pressure equations from the constitutive equation by treating the term $\nabla\cdot\boldsymbol{\tau}$ explicitly in the momentum equation. Further, the DEVSS-G term is decoupled from the velocity-pressure system and treated explicitly. An Operator Integration-Factor Splitting (OIFS) scheme [22] is used to treat the material derivative in the momentum equation. We make use of a 2nd-order OIFS2 approximation of the material derivative given by

$$\frac{D\mathbf{u}}{Dt} = \frac{\partial\mathbf{u}}{\partial t} + \mathbf{u}\cdot\nabla\mathbf{u} \approx \frac{1}{\Delta t}\left(\gamma_0\mathbf{u}^{n+1} - \sum_{q=0}^1 \alpha_q\tilde{\mathbf{u}}_q^{n+1}\right), \tag{16}$$

where $\gamma_0 = \frac{3}{2}$, $\alpha_0 = 2$ and $\alpha_1 = \frac{1}{2}$ are the multi-step coefficients for OIFS2 and $\tilde{\mathbf{u}}_0^{n+1}$ and $\tilde{\mathbf{u}}_1^{n+1}$ are solutions to the pure-advection initial value problems (IVP) associated with OIFS. The solutions of these IVPs are found using a 4th-order Runge-Kutta scheme.

Explicit terms are extrapolated at 2nd-order such that an approximation for an arbitrary function, $\mathbf{F}(\mathbf{X}, t)$ at time t^{n+1} is approximated by

$$\mathbf{F}^{n+1} \approx \sum_{q=0}^1 \beta_q\mathbf{F}^{n-q}, \tag{17}$$

where $\beta_0 = 2$, $\beta_1 = -1$ are the extrapolation coefficients. The resulting OIFS2/EX2 semi-discrete velocity-pressure system is

$$\frac{Re\gamma_0}{\Delta t}\mathbf{u}^{n+1} - (\beta+\theta)\nabla^2\mathbf{u}^{n+1} + \nabla p^{n+1} = \mathbf{f}^{n+1}$$
$$+ \sum_{q=0}^1\left(\frac{Re}{\Delta t}\alpha_q\tilde{\mathbf{u}}_q^{n+1} + \beta_q(\nabla\cdot\boldsymbol{\tau}^{n-q} - \theta\nabla\cdot\mathbf{G}^{n-q})\right), \tag{18}$$

$$\nabla\cdot\mathbf{u}^{n+1} + \mu\int_\Omega p^{n+1}d\Omega = 0. \tag{19}$$

For the constitutive equation we employ a hybrid backward difference and extrapolation (BDF/EX) scheme [23]. Consider a differential equation of the form

$$\frac{\partial\mathbf{X}}{\partial t}(\mathbf{X}, t) = \mathbf{F}_1(\mathbf{X}, t) + \mathbf{F}_2(\mathbf{X}, t), \tag{20}$$

where $\mathbf{F}_1(\mathbf{X}, t)$ is explicitly known at all time steps up to t^{n+1} and $\mathbf{F}_2(\mathbf{X}, t)$ is known only at time steps up to t^n. The 2nd-order BDF/EX approximation of (20) at time t^{n+1} is given by

$$\frac{\gamma_0\mathbf{X}^{n+1} - \sum_{q=0}^1\alpha_q\mathbf{X}^{n-q}}{\Delta t} = \mathbf{F}_1(\mathbf{X}^{n+1}) + \sum_{q=0}^1\beta_q\mathbf{F}_2(\mathbf{X}^{n-q}) \tag{21}$$

where γ_0, α_q and β_q are multi-step coefficients as given for OIFS2/EX2. The resulting BDF2/EX2 semi-discrete constitutive

equation is

$$\left(1 + We\frac{\gamma_0}{\Delta t}\right)\boldsymbol{\tau}^{n+1} - We\left(\boldsymbol{\tau}^{n+1} \cdot \nabla\mathbf{u}^{n+1} + \left(\nabla\mathbf{u}^{n+1}\right)^T \cdot \boldsymbol{\tau}^{n+1}\right)$$

$$= 2(1-\beta)\mathbf{d}^{n+1} + We\sum_{q=0}^{1}\left(\frac{\alpha_q}{\Delta t}\boldsymbol{\tau}^{n-q} - \beta_q\mathbf{u}^{n+1} \cdot \nabla\boldsymbol{\tau}^{n-q}\right)$$

$$-We\frac{\alpha}{(1-\beta)}\sum_{q=0}^{1}\beta_q\left(\boldsymbol{\tau}^{n-q}\right)^2. \tag{22}$$

4.1.1. Semi-implicit scheme

In order to improve stability we implement a semi-implicit scheme for the constitutive equation by applying a fixed-point iteration within each time step. Setting $\widetilde{\boldsymbol{\tau}}^0 = \boldsymbol{\tau}^n$, we solve iteratively the following BDF2/FPI semi-discrete system for $\widetilde{\boldsymbol{\tau}}^{i+1}$,

$$\left(1 + We\frac{\gamma_0}{\Delta t}\right)\widetilde{\boldsymbol{\tau}}^{i+1} - We\left(\widetilde{\boldsymbol{\tau}}^{i+1} \cdot \nabla\mathbf{u}^{n+1} + \left(\nabla\mathbf{u}^{n+1}\right)^T \cdot \widetilde{\boldsymbol{\tau}}^{i+1}\right)$$

$$= 2(1-\beta)\mathbf{d}^{n+1} + We\left(\sum_{q=0}^{1}\left(\frac{\alpha_q}{\Delta t}\boldsymbol{\tau}^{n-q}\right) - \mathbf{u}^{n+1} \cdot \nabla\widetilde{\boldsymbol{\tau}}^{i}\right)$$

$$-We\frac{\alpha}{1-\beta}\left(\widetilde{\boldsymbol{\tau}}^{i}\right)^2. \tag{23}$$

until $|\widetilde{\boldsymbol{\tau}}^{i+1} - \widetilde{\boldsymbol{\tau}}^{i}| < \delta$, where δ is some chosen tolerance. Once the tolerance is reached, typically after a handful of iterations, we set $\boldsymbol{\tau}^{n+1} = \widetilde{\boldsymbol{\tau}}^{i+1}$.

This scheme was preferred to the simpler BDF/EX2 scheme since the explicit nature of that scheme limited the maximum attainable Weissenberg number. When the BDF2/FPI scheme was used the maximum attainable Weissenberg number increased, allowing converged results for $We > 1$ to be obtained. The additional computational effort required for the fixed-point iteration is relatively small, so this is an economical method of achieving a semi-implicit discretization of the elastic stress.

4.2. Spatial discretisation

For the spatial discretisation of the equations we implement the spectral element method (SEM) which is based on the weak formulation of the governing equations. We define trial and test spaces

$$V := \left\{\mathbf{v} \in \left[H^1(\Omega)\right]^2 \mid \mathbf{v} = \mathbf{w} \text{ on } \partial\Omega_D\right\} \tag{24}$$

$$W := \left\{\mathbf{v} \in \left[H^1(\Omega)\right]^2 \mid \mathbf{v} = \mathbf{0} \text{ on } \partial\Omega_D\right\} \tag{25}$$

where $\mathbf{w}$ is the velocity condition on the Dirichlet boundary, $\partial\Omega_D$. In the case of the sphere benchmark problem $\partial\Omega_D = \Gamma^- \cup \Gamma^+ \cup \Gamma^W \cup \Gamma^C$ with $\mathbf{w}$ as defined in Section 3.

Given these spaces and given $\boldsymbol{\tau}$ and $\mathbf{G}$, the resulting weak form of Eqs. (6) and (7) is

Find $\mathbf{u} \in V$ and $p \in L_0^2(\Omega)$ such that,

$$Re\int_{\Omega}\mathbf{v} \cdot \frac{D\mathbf{u}}{Dt}\,d\Omega + (\beta+\theta)\int_{\Omega}\nabla\mathbf{u}:\nabla\mathbf{v}\,d\Omega - \int_{\Omega}p\nabla\cdot\mathbf{v}\,d\Omega$$

$$= \int_{\Omega}\mathbf{f}\cdot\mathbf{v}\,d\Omega - \int_{\Omega}\boldsymbol{\tau}:\nabla\mathbf{v}\,d\Omega$$

$$+\theta\int_{\Omega}\mathbf{G}:\nabla\mathbf{v}\,d\Omega \qquad \forall\,\mathbf{v} \in W \tag{26}$$

$$\int_{\Omega}q\nabla\cdot\mathbf{u}\,d\Omega = -\mu\int_{\Omega}q\,d\Omega\int_{\Omega}p\,d\Omega \quad \forall\,q \in L_0^2(\Omega). \tag{27}$$

4.2.1. Spectral element method

We discretise the physical domain, Ω, into K non-overlapping spectral elements such that $\Omega = \bigcup_{k=1}^{K}\Omega_k$ so that an integral over the domain may be decomposed into contributions over each spectral element. These contributions may then be mapped [24,25] from each element Ω_k onto a reference element, D, via the Jacobian of the mapping, J^k. Integrals in the weak formulation are approximated using Gauss-Lobatto-Legendre (GLL) quadrature rules. A spectral representation of the field variables is applied within the reference element with interpolation with respect to the GLL points

$$u_a^k(\xi,\eta) = \sum_{i=0}^{N}\sum_{j=0}^{N}\left(u_{ij}^k\right)_a h_i(\xi)h_j(\eta), \tag{28}$$

$$p^k(\xi,\eta) = \sum_{i=1}^{N-1}\sum_{j=1}^{N-1}p_{ij}^k\widetilde{h}_i(\xi)\widetilde{h}_j(\eta), \tag{29}$$

where the subscript a denotes the component of the vector field and $h_i(\xi)$ and $\widetilde{h}_i(\xi)$ are the velocity and pressure basis functions, respectively, defined by

$$h_i(\xi) = -\frac{(1-\xi^2)L_N'(\xi)}{N(N+1)L_N(\xi_i)(\xi-\xi_i)}, \qquad 0 \leq i \leq N, \tag{30}$$

and

$$\widetilde{h}_i(\xi) = -\frac{(1-\xi_i^2)L_N'(\xi)}{N(N+1)L_N(\xi_i)(\xi-\xi_i)}, \qquad 1 \leq i \leq N-1. \tag{31}$$

In these expressions $L_N(x)$ is the Legendre polynomial of degree N, and ξ_p is the pth GLL point in any one grid direction.

4.3. Discretisation of DEVSS-G terms

A spectral representation of the velocity gradient $\mathbf{G}$ within each spectral element is constructed using the internal GLL nodes in the same way as the treatment of the pressure. Using only the internal nodes means that $\mathbf{G}$ can be calculated in each element independently using an L^2-projection of the velocity gradient. Therefore, we do not need to construct the global matrix to solve for $\mathbf{G}$, thus reducing the computational effort required. This treatment also means that $\mathbf{G}$ is discontinuous across elements. While improving the computational efficiency this has also been found [26] to improve stability and accuracy when used in other numerical schemes.

The spectral representation of $\mathbf{G}$ in element Ω_k is given by

$$\mathbf{G}_{ab}^k(\xi,\eta) = \sum_{i=1}^{N-1}\sum_{j=1}^{N-1}\left(G_{ij}^k\right)_{ab}\widetilde{h}_i(\xi)\widetilde{h}_j(\eta), \tag{32}$$

where ab denotes the component of the tensor and $(G_{ij}^k)_{ab} = G_{ab}^k(\xi_i,\eta_j)$. Multiplying (8) by an appropriate test function, $\boldsymbol{\phi} \in [L^2(\Omega)]^5$, integrating over the whole domain and applying domain decomposition we obtain

$$\left(\sum_{k=1}^{K}\int_{\Omega_k}\mathbf{G}:\boldsymbol{\phi}\,d\Omega\right)_{ab} = \left(\sum_{k=1}^{K}\int_{\Omega_k}(\nabla\mathbf{u}):\boldsymbol{\phi}\,d\Omega\right)_{ab}. \tag{33}$$

Mapping onto the parent domain, applying the spectral representation of $\mathbf{G}$ and using GLL quadrature yields a linear system which may be expressed locally (in element Ω_k) for each component, ab, in the form

$$\widetilde{M}^k\mathbf{G}_{ab}^k = \widehat{\mathbf{d}}_{ab}^k \tag{34}$$

where $\widetilde{M}^k$ is the local pressure mass matrix and $\widehat{\mathbf{d}}_{ab}^k$ is the local vector containing the contribution from the ab component of the velocity gradient at each GLL point. Solution of this linear system yields the local values of $\mathbf{G}$ on each element, which are then used in turn for the solution of the velocity-pressure system.
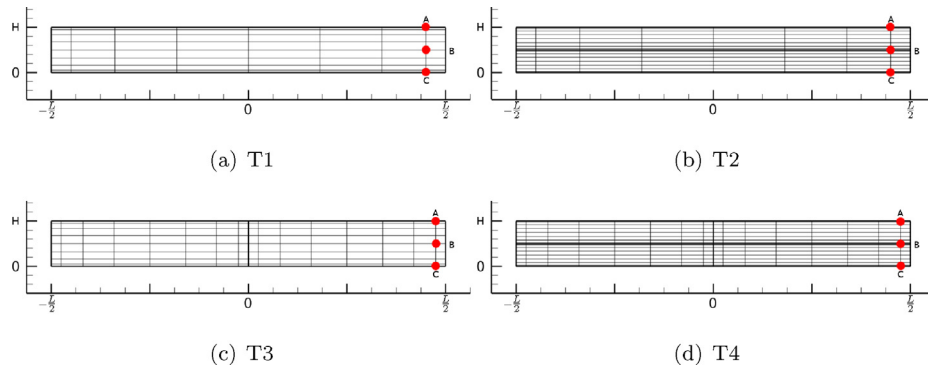
Fig. 1. Meshes T1–T4 used for simulations of start-up Poiseuille flow. Test points marked with a red dot at A, B and C. Each spectral element contains the local GLL-mesh for $N = 8$. (For interpretation of the references to colour in this figure legend, the reader is referred to the web version of this article.)
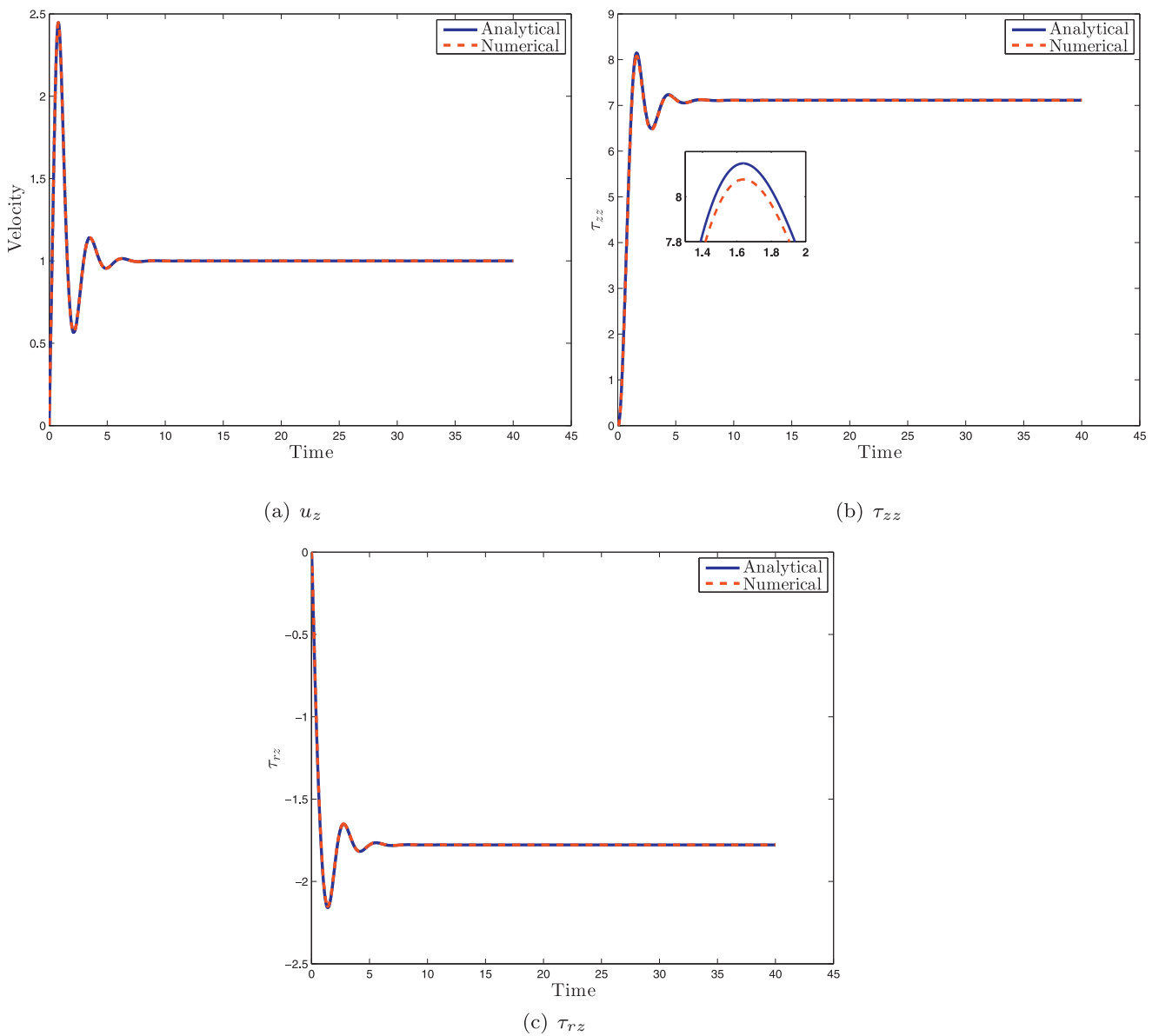
Fig. 2. Comparison of numerical and analytical solutions at the chosen test point for start-up of axisymmetric Poiseuille flow of an Oldroyd B fluid with $\beta = \frac{1}{9}$, $Re = 1$, $We = 1$. Parameters used are $\Delta t = 10^{-3}$, mesh $T1$, $L = 64$, $N = 8$.

(a) u_z

(b) τ_{zz}

(c) τ_{rz}
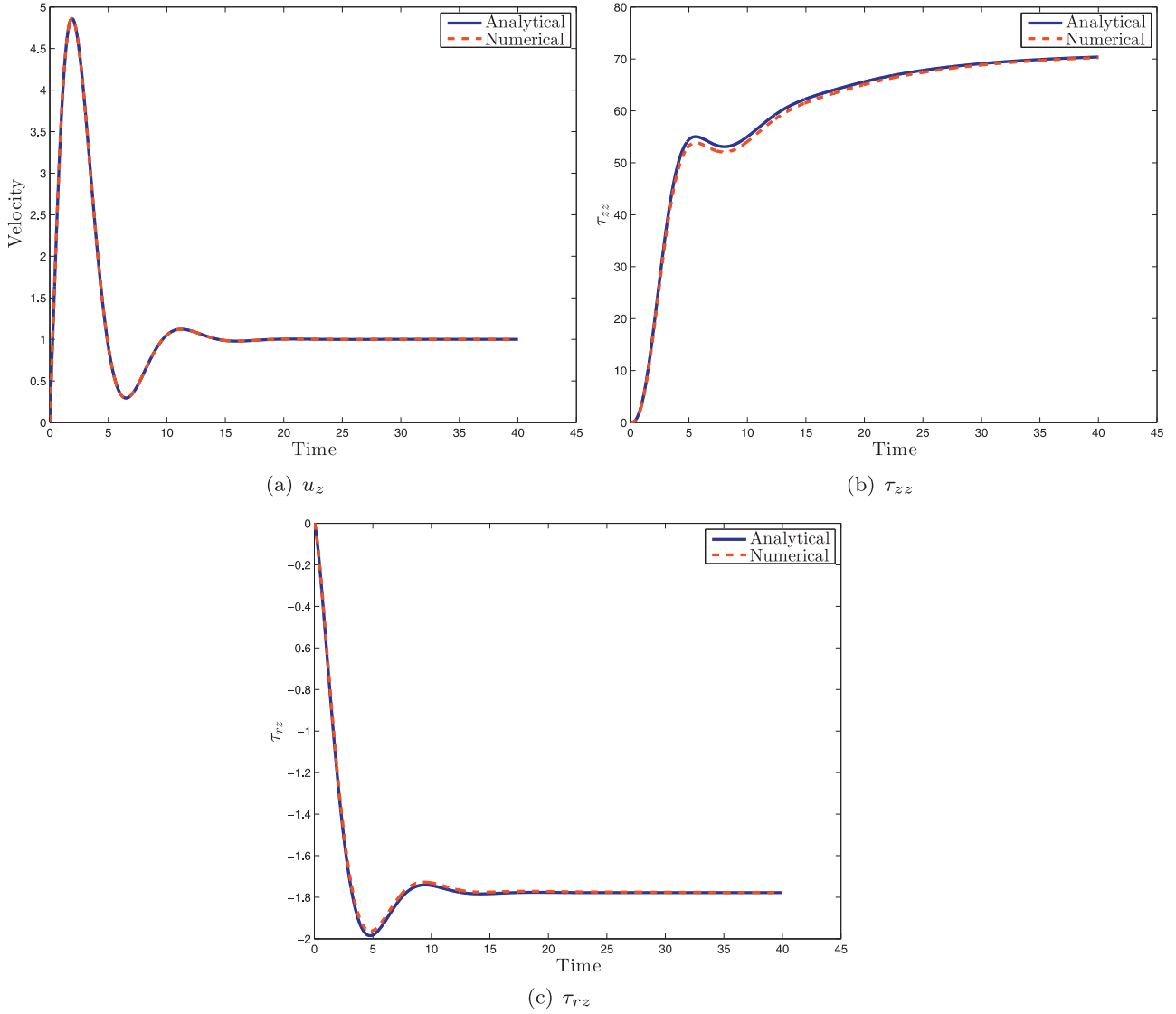
Fig. 3. Comparison of numerical and analytical solutions at the chosen test point for start-up of axisymmetric Poiseuille flow of an Oldroyd B fluid with $\beta = \frac{1}{9}$, $Re = 1$, $We = 10$. Parameters used are $\Delta t = 10^{-3}$, mesh $T1$, $L = 64$, $N = 8$.

Table 1
Time-averaged velocity error, E_u, at the test point using DEVSS-G, $\beta_s = 1$, for axisymmetric start-up flow of an Oldroyd B Fluid, $We = 1$, $\beta = \frac{1}{9}$, $Re = 1$, $L = 64$.

Mesh	Δt	N = 4	N = 8	N = 12	N = 16
T1	0.01	3.0658×10^{-3}	3.8300×10^{-4}	2.6086×10^{-4}	2.0473×10^{-4}
	0.001	2.6895×10^{-3}	4.8375×10^{-5}	9.3640×10^{-6}	7.6030×10^{-6}
	0.0001	2.6857×10^{-3}	4.6010×10^{-5}	7.4053×10^{-6}	6.1005×10^{-6}
T2	0.01	2.5098×10^{-4}	2.7530×10^{-4}	2.6250×10^{-4}	2.0469×10^{-4}
	0.001	1.0347×10^{-4}	8.7187×10^{-6}	8.0995×10^{-6}	7.7975×10^{-6}
	0.0001	1.0297×10^{-4}	7.3983×10^{-6}	5.8806×10^{-6}	6.1266×10^{-6}
T3	0.01	3.4506×10^{-3}	4.2757×10^{-4}	3.0421×10^{-4}	3.0489×10^{-4}
	0.001	2.9456×10^{-3}	5.0135×10^{-5}	1.0230×10^{-5}	9.5129×10^{-6}
	0.0001	2.9402×10^{-3}	4.7455×10^{-5}	8.0047×10^{-6}	7.3162×10^{-6}
T4	0.01	3.4725×10^{-4}	3.0445×10^{-4}	3.0533×10^{-4}	3.0443×10^{-4}
	0.001	1.0810×10^{-4}	9.7587×10^{-6}	9.0657×10^{-6}	9.2622×10^{-6}
	0.0001	1.0637×10^{-4}	8.2214×10^{-6}	6.8879×10^{-6}	7.7592×10^{-6}

4.4. Discontinuous Galerkin treatment of constitutive equation

We solve the constitutive equation spatially in strong form at each GLL point separately within each spectral element. This gives rise to a 4×4 linear system to solve, with the entries of the system being determined by the values of the velocity gradient and values of the elastic stress at previous time steps. The solution at these points allows us to use the spectral representation on each element

$$\tau_{ab}^e(\xi, \eta) = \sum_{i=0}^{N} \sum_{j=0}^{N} \left(\tau_{ab}^e\right)_{ij} h_i(\xi) h_j(\eta). \tag{35}$$
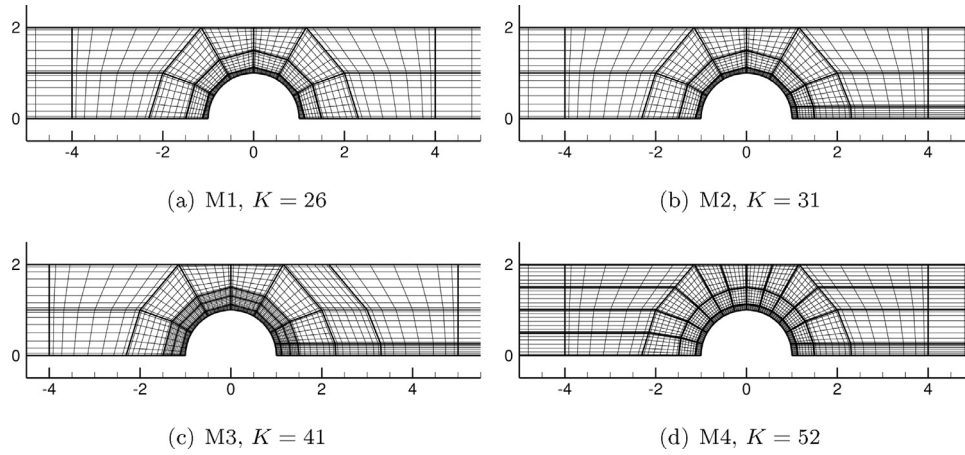
Fig. 4. Meshes M1–M4. Each spectral element contains the local GLL-mesh with $N = 8$.

Table 2
Drag factor for uniform flow of an Oldroyd B fluid past a fixed sphere in a cylinder with $Re = 0.01$ and $\beta = \frac{1}{2}$. Performed on mesh M1 with timestep, $\Delta t = 10^{-4}$ using DEVSS-G. Results from simulations which reached the time limit but did not meet the stopping criterion in Eq. (54) are marked with an asterisk.

We	N = 15	N = 16	N = 17	N = 18
0.1	5.906026	5.906027	5.906027	5.906027
0.2	5.808245	5.808245	5.808245	5.808245
0.3	5.694340	5.694340	5.694340	5.694340
0.4	5.586113	5.586113	5.586113	5.586113
0.5	5.491800	5.491800	5.491800	5.491800
0.6	5.413134	5.413133	5.413133	5.413132
0.7	5.349204*	5.349213	5.349213	5.349212

Table 3
Drag factor for uniform flow of an Oldroyd B fluid past a fixed sphere in a cylinder with $Re = 0.01$ and $\beta = \frac{1}{2}$. Performed on mesh M2 with timestep, $\Delta t = 10^{-4}$ using DEVSS-G. Results from simulations which reached the time limit but did not meet the stopping criterion in Eq. (54) are marked with an asterisk.

We	N = 13	N = 14	N = 15	N = 16
0.1	5.906026	5.906027	5.906027	5.906027
0.2	5.808245	5.808245	5.808245	5.808245
0.3	5.694340	5.694340	5.694340	5.694340
0.4	5.586113	5.586113	5.586113	5.586113
0.5	5.491801	5.491801	5.491800	5.491800
0.6	5.413131	5.413134	5.413134	5.413133
0.7	5.349203	5.349211	5.349213	5.349213
0.8	5.298236	5.298250	5.298259	5.298262
0.9	5.258296	5.258318	5.258334	5.258343
1	5.227584	5.227611	5.227635	5.227653
1.1	5.204528*	5.204543*	5.204586*	5.204597*
1.2	5.187791*	5.188075*	5.187858*	5.188740*

Table 4
Drag factor for uniform flow of an Oldroyd B fluid past a fixed sphere in a cylinder with $Re = 0.01$ and $\beta = \frac{1}{9}$. Performed on mesh M2 with timestep, $\Delta t = 10^{-4}$ using DEVSS-G. Results from simulations which reached the time limit but did not meet the stopping criterion in Eq. (54) are marked with an asterisk.

We	N = 13	N = 14	N = 15	N = 16
0.1	5.872271	5.872271	5.872271	5.872271
0.2	5.693800	5.693800	5.693800	5.693800
0.3	5.483275	5.483275	5.483275	5.483275
0.4	5.280605	5.280604	5.280604	5.280604
0.5	5.101474	5.101472	5.101471	5.101471
0.6	4.949510	4.949507	4.949505	4.949504
0.7	4.823299	4.823296	4.823292	4.823289
0.8	4.719717	4.719711	4.719705	4.719700
0.9	4.635359	4.635348	4.635335	4.635326
1	4.567085*	4.567059*	4.567061*	4.567092*
1.1	4.515530*	4.511213*	4.512671*	4.520344*

Table 5
Drag factor for uniform flow of an Oldroyd B fluid past a fixed sphere in a cylinder with $Re = 0.01$ and $\beta = \frac{1}{2}$. Performed on meshes M3 and M4 with timestep, $\Delta t = 10^{-4}$ using DEVSS-G. Results from simulations which reached the time limit but did not meet the stopping criterion in Eq. (54) are marked with an asterisk.

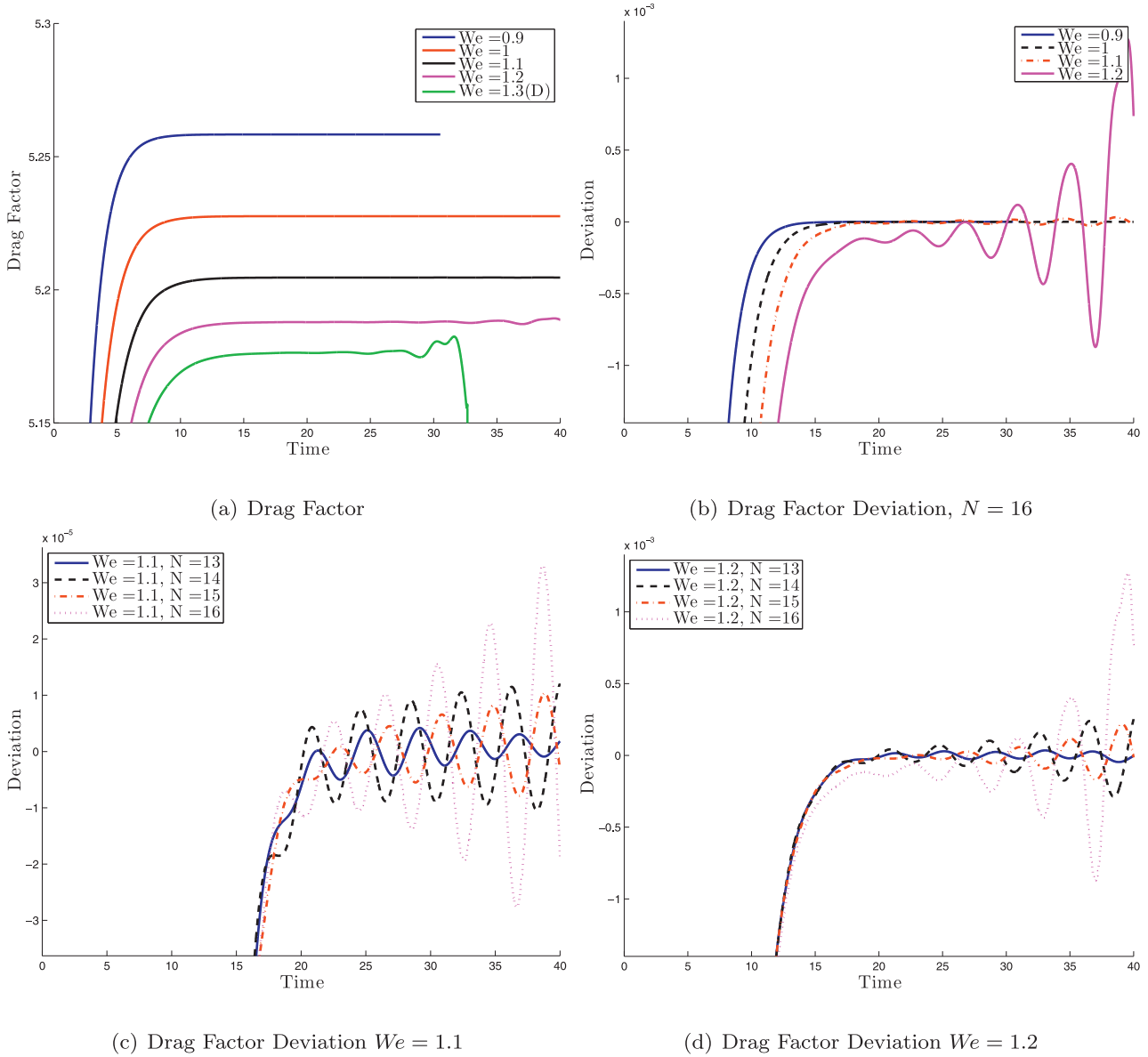| We	N = 13	N = 14	N = 15	N = 16
Mesh M3				
0.9	5.258340	5.258349	5.258348	5.258345
1	5.227636*	5.227660*	5.227668	5.227666*
1.1	5.204575*	5.204618*	5.204640*	5.204649*
1.2	5.187806*	5.187870*	5.187914*	5.187959*
Mesh M4				
0.9	5.258296	5.258319	5.258335	5.258344
1	5.227584*	5.227611*	5.227635*	5.227652*
1.1	5.204530*	5.204569*	5.204586*	5.204596*
1.2	5.187791*	5.188074*	5.187878*	5.188702*

The only coupling between elements is via the convection term, which we treat using a discontinuous Galerkin (DG) method allowing for solution of the system on both an element-by-element and GLL point-by-point basis.

The discontinuous Galerkin (DG) method was first introduced in the 1970s for use with the neutron transport equation by Lesaint and Raviart [27], but was eventually used for the simulation of viscoelastic fluid flows by Fortin and Fortin [28]. In their method, the stress approximation was allowed to be discontinuous across elements. This allowed the stress to be solved on an element-by-element basis which can substantially reduce computational costs. A further advantage, when compared to continuous Galerkin interpolations, is that the velocity-stress compatibility

condition is satisfied easily. In the following description we follow the presentation by Owens and Phillips [4].

4.4.1. Derivation of DG treatment of convection term

A streamline upwinded discontinuous Galerkin (DG) treatment of the constitutive equation is utilised, which allows the stress to be discontinuous across elements. The stress between elements then only interacts in operations involving shared elemental boundaries. We reconsider the convective derivative, multiplying by an appropriate stress test function $\mathbf{S} \in \Sigma = \left[L^2(\Omega) \right]^5$ and integrating over Ω. The weak form of the convective derivative may

(a) Drag Factor

(b) Drag Factor Deviation, $N = 16$

(c) Drag Factor Deviation $We = 1.1$

(d) Drag Factor Deviation $We = 1.2$

Fig. 5. Evolution of the drag factor for uniform flow of an Oldroyd B fluid past a fixed sphere in a cylinder with $Re = 0.01$ and $\beta = \frac{1}{2}$ performed on mesh M2, with timestep, $\Delta t = 10^{-4}$ using DEVSS-G. The deviation from an approximate average value is computed.

be written in the form

$$\int_{\Omega} (\mathbf{u} \cdot \nabla \boldsymbol{\tau}) : \mathbf{S} \, d\Omega = \sum_{k=1}^{K} \int_{\Omega_k} (\mathbf{u} \cdot \nabla \boldsymbol{\tau}) : \mathbf{S} \, d\Omega_k. \tag{36}$$

Applying the divergence theorem to the first term on the right-hand side, we obtain,

$$\sum_{k=1}^{K} \int_{\Omega_k} (\mathbf{u} \cdot \nabla \boldsymbol{\tau}) : \mathbf{S} \, d\Omega_k = \sum_{k=1}^{K} \int_{\Gamma_k} (\mathbf{n} \cdot \mathbf{u}) \boldsymbol{\tau} : \mathbf{S} \, d\Gamma_k$$
$$- \sum_{k=1}^{K} \int_{\Omega_k} (\mathbf{u} \cdot \nabla \mathbf{S}) : \boldsymbol{\tau} \, d\Omega_k. \tag{37}$$

Consider a particular element, Ω_k, and suppose that there is a point, $\mathbf{x}$, on the edge of that element, $\bar{\Omega}_k$ which is shared with the edge of a neighbouring element, $\bar{\Omega}_l$. Since stress is allowed to be discontinuous across elements, the value of the elastic stress is not necessarily the same at an element interface when evaluated using approximations in adjoining elements.

With this in mind, we denote by $\boldsymbol{\tau}^e(\mathbf{x})$ the value of the elastic stress at $\mathbf{x} \in \bar{\Omega}_l$ and by $\boldsymbol{\tau}^i(\mathbf{x})$ the value at $\mathbf{x} \in \bar{\Omega}_k$. We call these the external and internal stress tensors, respectively. We now define
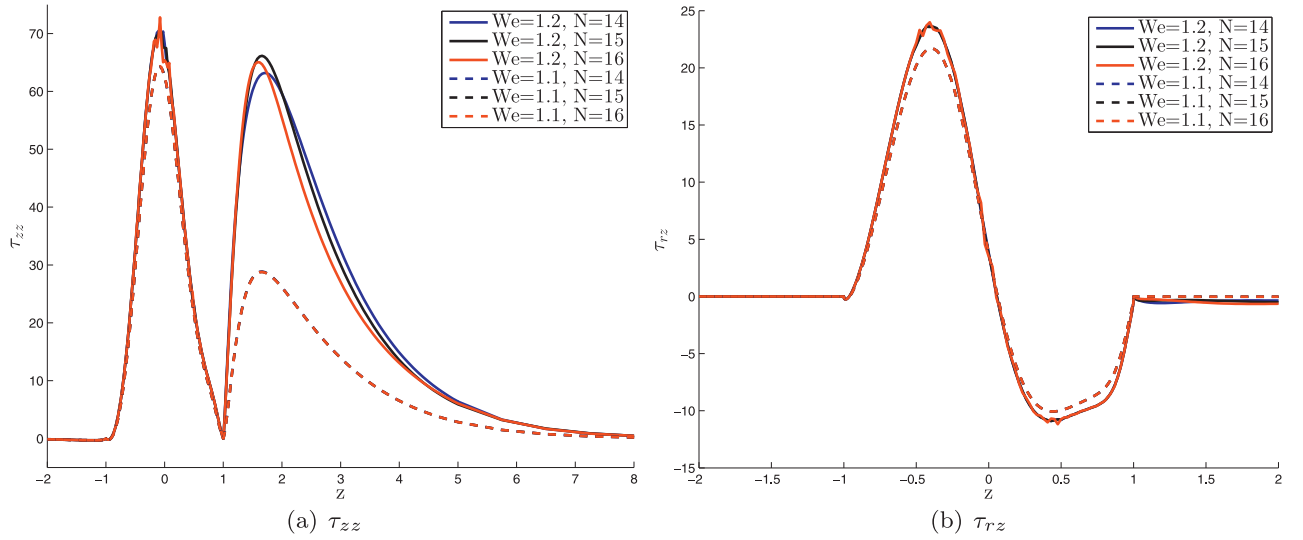
$$\boldsymbol{\tau} = \begin{cases} \alpha_{DG} \boldsymbol{\tau}^e + (1 - \alpha_{DG}) \boldsymbol{\tau}^i & \text{on } \Gamma_k^- \setminus \Gamma^-, \\ \alpha_{DG} \boldsymbol{\tau}^i + (1 - \alpha_{DG}) \boldsymbol{\tau}^e & \text{on } \Gamma_k^+ \setminus \Gamma^+, \end{cases} \tag{38}$$

for some upwinding parameter, $\alpha_{DG} \in [0, 1]$, where $\alpha_{DG} = 1$ corresponds to a fully upwinded formulation.

Substituting (38) into (37), applying integration by parts a second time and using the divergence theorem on the last term with $\boldsymbol{\tau} \equiv \boldsymbol{\tau}^i$ on $\Gamma_k \setminus \Gamma^-$ we obtain

$$\sum_{k=1}^{K} \int_{\Omega_k} (\mathbf{u} \cdot \nabla \boldsymbol{\tau}) : \mathbf{S} \, d\Omega_k = \sum_{k=1}^{K} \int_{\Omega_k} (\mathbf{u} \cdot \nabla \boldsymbol{\tau}) : \mathbf{S} \, d\Omega_k$$
$$+ \alpha_{DG} \sum_{k=1}^{K} \int_{\Gamma_k^- \setminus \Gamma^-} (\mathbf{n} \cdot \mathbf{u}) [\![\boldsymbol{\tau}]\!] : \mathbf{S} \, d\Gamma_k$$
$$+ (1 - \alpha_{DG}) \sum_{k=1}^{K} \int_{\Gamma_k^+ \setminus \Gamma^+} (\mathbf{n} \cdot \mathbf{u}) [\![\boldsymbol{\tau}]\!] : \mathbf{S} \, d\Gamma_k \tag{39}$$

(a) τ_{zz}

(b) τ_{rz}

Fig. 6. Axial components of the polymeric stress along the wall of symmetry for uniform flow of an Oldroyd B fluid past a fixed sphere in a cylinder with $Re = 0.01$ and $\beta = \frac{1}{2}$ performed on mesh M2, with timestep, $\Delta t = 10^{-4}$ using DEVSS-G.

where $[\![\boldsymbol{\tau}]\!] \equiv \boldsymbol{\tau}^e - \boldsymbol{\tau}^i$ represents the jump in stress between elements. By replacing the weak treatment of the convected derivative in the constitutive equation with (39) we obtain the DG formulation.

4.4.2. Discretisation of convective term by DG method

Up to this point, the discretisation of the constitutive equation has been performed in strong form. The DG method requires integration in order to create the jump term, so we require a way to incorporate this change without impacting on the previously described calculation of elastic stress. This can be achieved if we calculate the DG convection term separately. First, we introduce an intermediate variable

$$\widehat{\boldsymbol{\tau}} = \mathbf{u} \cdot \nabla \boldsymbol{\tau}. \tag{40}$$

Given that, at any particular timestep, we treat the convection terms explicitly, we calculate an approximation of $\widehat{\boldsymbol{\tau}}$ for a given velocity and elastic stress field.

Setting $\alpha_{DG} = 1$ in (39) we note that we may calculate $\widehat{\boldsymbol{\tau}}$ on an element-by-element basis. Dropping the summation over all elements, we write the SEM approximation of each component, ab, of the left-hand side of the DG system, locally, in terms of the matrix-vector multiplication

$$\left(\int_{\Omega_k} \widehat{\boldsymbol{\tau}}(\mathbf{x}) : \mathbf{S} d\Omega \right)_{ab} = \left(\int_D \widehat{\boldsymbol{\tau}}^k(\xi, \eta) : \mathbf{S} \det \mathbf{J}^k \, d\xi d\eta \right)_{ab} \approx M^k \widehat{\boldsymbol{\tau}}^k_{ab}, \tag{41}$$

where entries corresponding to a global inflow node must be set to zero and removed from the linear system.

Next, each non-zero component of the integral on the right-hand side of (39) may be expressed locally by means of the matrix-vector multiplication

$$\left(\int_{\Omega_k} (\mathbf{u} \cdot \nabla \boldsymbol{\tau}) : \mathbf{S} \, d\Omega \right)_{ab} = \left(\int_D \left(\mathbf{u}^k \cdot \nabla \boldsymbol{\tau}^k \right) : \mathbf{S} \det \mathbf{J}^k \, d\xi d\eta \right)_{ab} \approx \widehat{E}^k \boldsymbol{\tau}^k_{ab}, \tag{42}$$

where

$$\left(\widehat{E}^k \right)_{kl,ij} = \left(u_r^k \right)_{kl} \left(E_r^k \right)_{ij,kl} + \left(u_z^k \right)_{kl} \left(E_z^k \right)_{ij,kl}. \tag{43}$$

This leaves only a term for the boundary integral, which may be expressed by

$$\left(\int_{\Gamma_k^- \backslash \Gamma^-} (\mathbf{n} \cdot \mathbf{u}) [\![\boldsymbol{\tau}^k]\!] : \mathbf{S} \, d\Gamma \right)_{ab}$$
$$= \left(\sum_{m=1}^{4} \int_{D_{\bar{m}} \backslash \Gamma^-} \left(\mathbf{n}^{k_m} \cdot \mathbf{u}^k \right) [\![\boldsymbol{\tau}^k]\!] : \mathbf{S} \, \det \mathbf{J}^{k_m} d\xi \right)_{ab} \approx \left(B_{DG}^k \right)_{ab}, \tag{44}$$

where the sum over m refers to the four edges of the parent element and $\mathbf{J}^{k_m}$ is the Jacobian of the edge mapping from edge m of element Ω_k to the parent edge $[-1, 1]$. The entries of $(B_{DG}^k)_{ab}$ are given by

$$\left[\left(B_{DG}^k \right)_{ab} \right]_{ij} = \sum_{(\xi_i, \eta_j) \in D_{\bar{m}}} \left(\left(u_z^k \right)_{ij} \left(n_z^{k_m} \right)_{ij} + \left(u_r^{k_m} \right)_{ij} \left(n_r^{k_m} \right)_{ij} \right)$$
$$\times [\![\tau_{ab}^k]\!]_{ij} \det \left(\mathbf{J}^{k_m} \right)_{m_{ij}} w_{m_{ij}} \tag{45}$$

with $0 \leq i, j \leq N$ and where m_{ij} is the 1-D GLL edge point corresponding to the 2-D GLL grid point (ξ_i, η_j). Note that the value of $\left[\left(B_{DG}^k \right)_{ab} \right]_{ij}$ is zero unless the GLL node ij lies on an elemental inflow interface.

The DG contribution to each component of $\widehat{\tau}_{ab}^k$ on each element Ω_k may then be calculated by solving the following linear system

$$M^k \widehat{\tau}_{ab}^k = \widehat{E}^k \tau_{ab}^k + \left(B_{DG}^k \right)_{ab}. \tag{46}$$

This system is trivial to solve for the choice of stress test function since the matrix M^k is diagonal. The contribution of each component is then included on the appropriate right-hand side of the constitutive equation. When using the semi-iterative scheme, the DG contribution is updated at every iteration.

4.5. Global linear system

Summing contributions over all elements and accounting for shared boundaries the global matrix for the velocity-pressure system can be assembled. The global matrix may be written in block form, with matrices for each component of the co-ordinate system, a, associated with operators within the governing equations. The resulting block system is
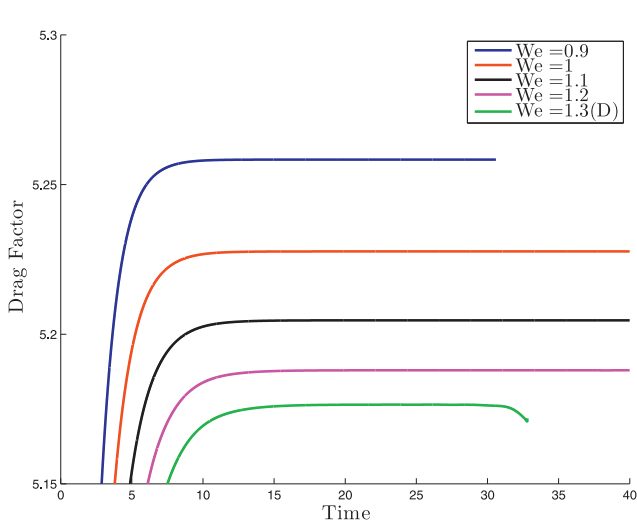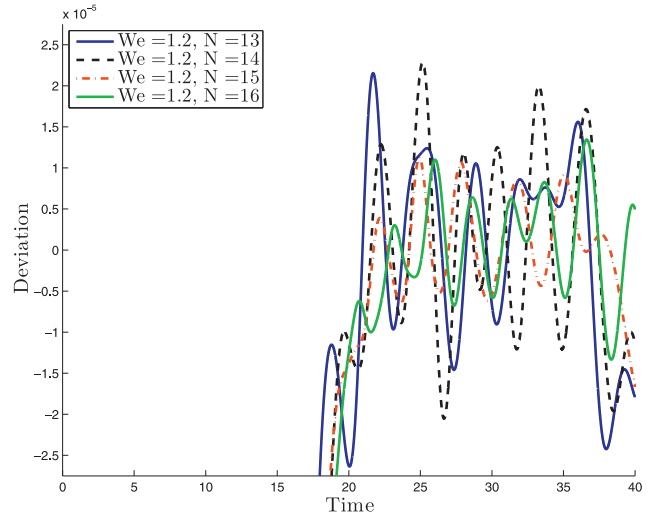
(a) Drag Factor, M4
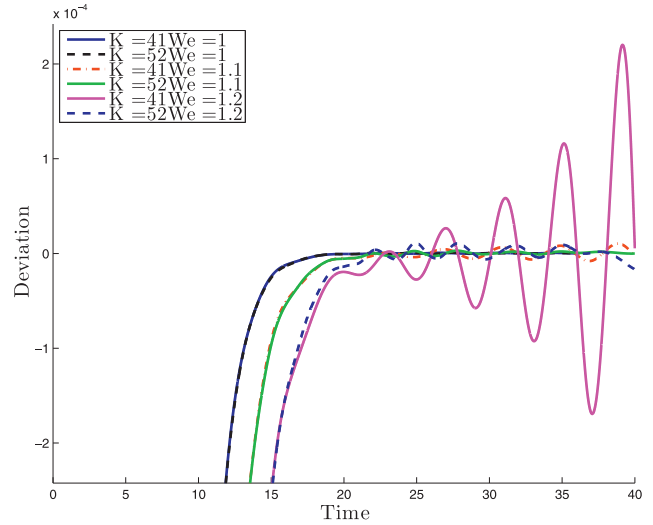
(b) Drag Factor Deviation, M3 and M4.
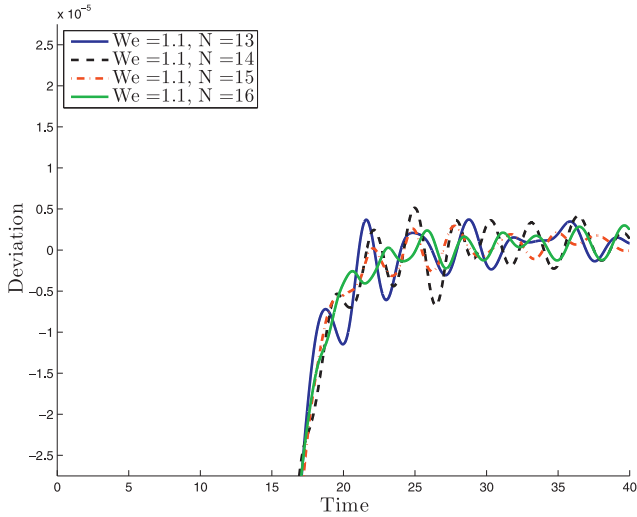
(c) Drag Factor Deviation $We = 1.1$, M4.

(d) Drag Factor Deviation $We = 1.2$, M4

Fig. 7. Evolution of the drag factor for uniform flow of an Oldroyd B fluid past a fixed sphere in a cylinder with $Re = 0.01$ and $\beta = \frac{1}{2}$. Performed on meshes M3 and M4, $N = 16$, with timestep, $\Delta t = 10^{-4}$ using DEVSS-G. The deviation is computed by finding an approximate average value.

$$
\begin{pmatrix}
\frac{Re\gamma_0}{\Delta t} M_r + \beta(A_r + A_\theta) & 0 & -(B_r + B_\theta) \\
0 & \frac{Re\gamma_0}{\Delta t} M_z + \beta A_z & -B_z \\
-(B_r + B_\theta)^T & -B_z^T & \mu C
\end{pmatrix}
\begin{pmatrix}
\mathbf{u}_r^{n+1} \\
\mathbf{u}_z^{n+1} \\
\mathbf{p}^{n+1}
\end{pmatrix}
$$

$$
=
\begin{pmatrix}
\widehat{\mathbf{f}}_r^{n+1} \\
\widehat{\mathbf{f}}_z^{n+1} \\
\widehat{\mathbf{g}}^{n+1}
\end{pmatrix}
\tag{47}
$$

where M_a are the mass matrices, A_a the stiffness matrices, B_a the gradient matrix, B_a^T the divergence matrices and C the matrix associated with the integral of pressure. The components of the right-hand side are given by

$$
\widehat{\mathbf{f}}_r^{n+1} = M_r \mathbf{f}_r^{n+1} + \frac{Re}{\Delta t} \sum_{q=0}^{1} \alpha_q M_r \tilde{\mathbf{u}}_{r_q}^{n+1} + \sum_{q=0}^{1} \beta_q \left(E_r \left(\boldsymbol{\tau}_{rr}^{n-q} + \theta \mathbf{G}_{rr}^{n-q} \right) \right.
$$
$$
\left. + E_z \left(\boldsymbol{\tau}_{rz}^{n-q} + \theta \mathbf{G}_{rz}^{n-q} \right) + E_\theta \left(\boldsymbol{\tau}_{\theta\theta}^{n-q} + \theta \mathbf{G}_{\theta\theta}^{n-q} \right) \right),
\tag{48}
$$

$$
\widehat{\mathbf{f}}_z^{n+1} = M_z \mathbf{f}_z^{n+1} + \sum_{q=0}^{1} \left(Re \frac{\alpha_q}{\Delta t} M_z \tilde{\mathbf{u}}_{z_q}^{n+1} + \beta_q \left(E_r \boldsymbol{\tau}_{rz}^{n-q} + E_z \boldsymbol{\tau}_{zz}^{n-q} \right) \right), \tag{49}
$$

$$
\widehat{\mathbf{g}}^{n+1} = 0. \tag{50}
$$

Known boundary conditions are incorporated into the right-hand side of (47) where required.

We solve the linear system using the PARDISO sparse direct solver contained in the Intel MKL library [29]. Since the geometry does not change between time steps the matrices remain constant which allows us to pre-compute and store the LDL^T decomposition of the global matrix, using only forward and back substitution for the subsequent solves. In the axisymmetric geometry, where memory requirements are not prohibitively expensive, the use of an efficient direct solver is preferable to the use of an iterative solver. The dominant computational cost of performing the factorization of the global matrix, $\mathcal{O}(M^3)$ for a system of size M, needs only be performed once and the cost of each subsequent time step is significantly less at $\mathcal{O}(M^2)$. For a fully three-dimensional
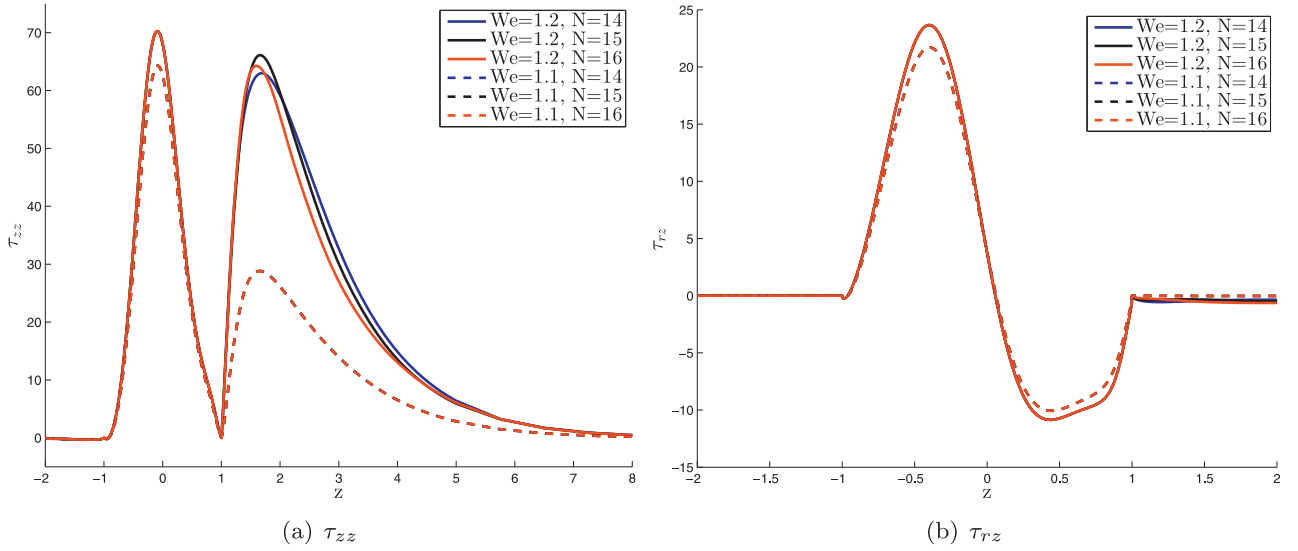
Fig. 8. Axial stress components along the wall of symmetry for uniform flow of an Oldroyd B fluid past a fixed sphere in a cylinder with $Re = 0.01$ and $\beta = \frac{1}{2}$. Performed on mesh M4, with timestep, $\Delta t = 10^{-4}$ using DEVSS-G.

problem the use of a direct solver would be impractical due to the memory required to store such a factorisation. In this case a multi-level iterative method would be more economical.

5. Results

5.1. Start-up of Poiseuille flow

As an initial benchmark problem we consider Poiseuille flow in a cylindrical pipe of length L and radius H. For an Oldroyd B fluid there is an analytical solution for the start-up of Poiseuille flow derived by Waters and King [30]. The non-trivial component of velocity at time t is given (in our non-dimensionalisation, adapted from [31]) by

$$u_z(r,t) = \left(1 - r^2\right) - 8 \sum_{n=1}^{\infty} \frac{J_0(rZ_n)}{J_1(Z_n)Z_n^3} \exp\left(-\frac{\alpha_n t}{2El}\right) G_n(t), \qquad (51)$$

where Z_n is the nth real and positive root of the Bessel function of zero order, J_0, $El = \frac{We}{Re}$ is the elasticity number,

$$G_n(t) = \cosh\left(\frac{\beta_n t}{2El}\right) + \left[\frac{1 + Z_n^2 El(\beta - 2)}{\beta_n}\right] \sinh\left(\frac{\beta_n t}{2El}\right), \qquad (52)$$

and

$$\alpha_n = 1 + El\beta Z_n^2, \quad \beta_n = \left[(1 + El\beta Z_n)^2 - 4ElZ_n^2\right]^{1/2}, \qquad (53)$$

with β the viscosity ratio.

While the planar solution to this problem has been widely used as a validation tool for numerical schemes, the axisymmetric version has received less attention with the only statement of the stress components of the problem to be found in the paper by Ryan and Dutta [32] who derived an expression for the shear stress. We make comparisons primarily with the velocity for the purposes of validation, although we compare our stress solution with an approximate analytical solution for the elastic stress by combining knowledge of the exact velocity solution with a numerical approximation of the temporal derivatives of elastic stress. We are able to compute the velocity and its gradients, so we make use of a BDF scheme to compute the elastic stress using previously computed values (and the initial zero value to start).

We fix the length of the pipe to be $L = 64$ and the radius to be $H = 1$. We impose zero initial conditions for stress and velocity and apply the analytical solution for velocity at inflow and

outflow and for stress only at inflow. No-slip and no-penetration conditions are imposed on the wall and symmetry wall conditions are applied at the centre of the cylinder, which is the bottom of our computational domain. We present the evolution of u_r, τ_{rz} and τ_{zz} at the test points marked C (centre line) and A (top wall), respectively, in Fig. 1. We choose $Re = 1$ and $\beta = \frac{1}{9}$ and consider $We = 1, 10$. For the computation we consider four meshes, T1–T4, shown in Fig. 1 and consider $N = 4, 8, 12$ and 16. We set our temporal timestep to be $\Delta t = 10^{-3}$ and stop the stimulation after 40 time units.

Fig. 2 shows the computed non-zero values of velocity (point A) and stress (point C) at their respective test points (marked in Fig. 1) at $We = 1$ for moderate N on the mesh T1. There is excellent agreement with the velocity and only the computed value of τ_{zz} overshoots the analytical solution in a noticeable manner. On a single element, mesh T1, with $N = 8$, $L = 16$ and $\Delta t = 10^{-3}$, the difference between our solution and the computed analytical solution at the first peak is -3.7764×10^{-5} (-0.00154%) for velocity, 0.0708 (0.88%) for τ_{zz} and 0.0086 (0.4%) for τ_{rz}. The largest error is in the axial component of stress and is in line with results for the planar case [33].

Fig. 3 shows the computed non-zero values of velocity and stress at their respective test points at $We = 10$, which was chosen to test the stability of the scheme at higher values of We. Again there is good agreement for the velocity, although the error is now more pronounced for the stress with the numerical approximation slightly undershooting the analytical solution at the first turning point.

Table 1 shows the time-averaged velocity error at $We = 1$ over the whole domain for each mesh for different values of N. Focusing on the single element results at high N, the second-order convergence of the temporal scheme is clear when decreasing the timestep from 0.01 to 0.001. Similarly, fixing the timestep at 0.001 we see an improvement with increasing N.

We further note that the length of the channel, L, has an impact on the stability of the numerical solution. We chose $L = 64$ to eliminate these, but for shorter channel lengths, we see similar behaviour to that observed by Van Os and Phillips [33]. Further, one can see in Table 1 that increasing the number of downstream elements (from mesh T1 to mesh T3) does not result in any improvement in accuracy. In fact, increasing the number of downstream elements for shorter channel lengths also impacted on the
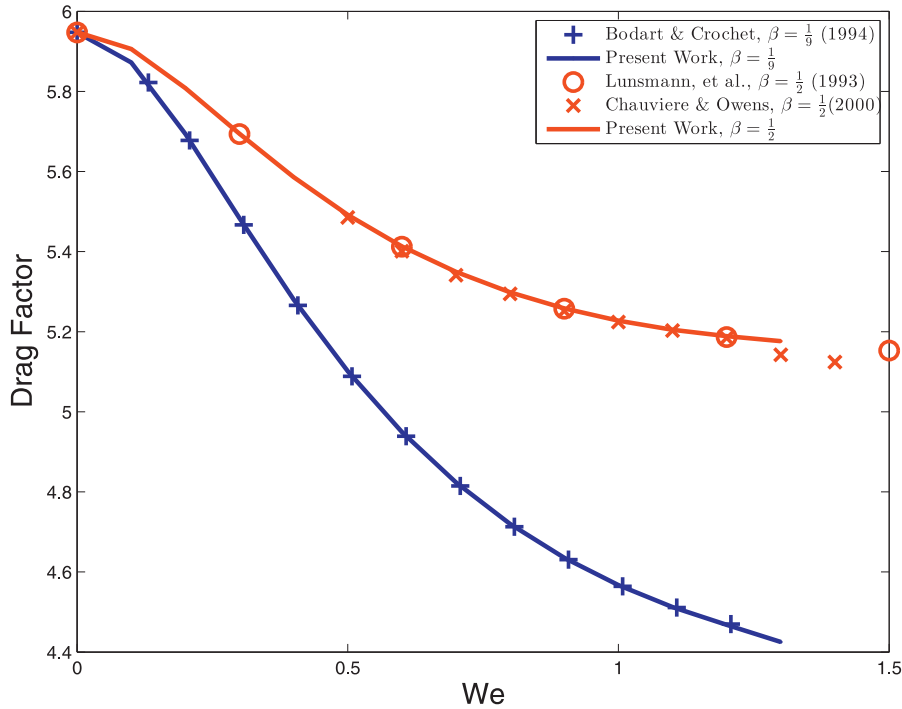
Fig. 9. Comparison of results for the benchmark flow past a fixed sphere in a cylinder for an Oldroyd B fluid with the literature. Values for present work are taken from Tables 6 and 7.

Table 6

Drag factor for uniform flow of an Oldroyd B fluid past a fixed sphere in a cylinder with $Re = 0.01$, $\beta = \frac{1}{9}$. Comparison of results taken from Table 4 and additional simulations performed on mesh M4 at $N = 16$. Results from simulations which reached the time limit but did not meet the stopping criterion in Eq. (54) are marked with an asterisk. Results which subsequently diverged are marked with a (D), these values are calculated at the timestep with the minimum value of S^n.

Present Work		Bodart & Crochet [10]	
We	Drag Factor	We	Drag Factor
0	5.9478	0	5.9475
0.1	5.8723	0.1318750	5.8224
0.2	5.6938	0.2078125	5.6775
0.3	5.4833	0.3078125	5.4666
0.4	5.2806	0.4078125	5.2655
0.5	5.1015	0.5078125	5.0885
0.6	4.9495	0.6078125	4.9388
0.7	4.8233	0.7078125	4.8147
0.8	4.7197	0.8078125	4.7131
0.9	4.6353	0.9078125	4.6306
1	4.5670*	1.0078125	4.5642
1.1	4.5121*	1.1078125	4.5112
1.2	4.4680*	1.2078125	4.4697
1.3	4.4252(D)	1.3078125	–

Table 7

Drag factor for uniform flow of an Oldroyd B fluid past a fixed sphere in a cylinder with $Re = 0.01$, $\beta = \frac{1}{2}$. Comparison of results taken from Tables 3 and 5. Results from simulations which reached the time limit but did not meet the stopping criterion in Eq. (54) are marked with an asterisk. Results which subsequently diverged are marked with a (D), these values are calculated at the timestep with the minimum value of S^n.

We	Present work	Chauvière & Owens [5]	Lunsmann et al. [9]
0	5.9478	5.9475	5.9472
0.1	5.9060	–	–
0.2	5.8082	–	–
0.3	5.6943	–	5.6937
0.4	5.5861	–	–
0.5	5.4918	5.4852	–
0.6	5.4131	5.4009	5.4123
0.7	5.3492	5.3411	–
0.8	5.2983	5.2945	–
0.9	5.2583	5.2518	5.2572
1	5.2276	5.224	–
1.1	5.2046*	5.2029	–
1.2	5.1887*	5.1842	5.1865
1.3	5.1765(D)	5.1421	–
1.4	–	5.1240	–
1.5	–	–	5.1529

stability of the solution, which also agrees with the observations of Van Os and Phillips [33]. Conversely, increasing the number of cross-stream elements (from mesh T1 to mesh T2) does result in an increase in accuracy and does not impact on stability.
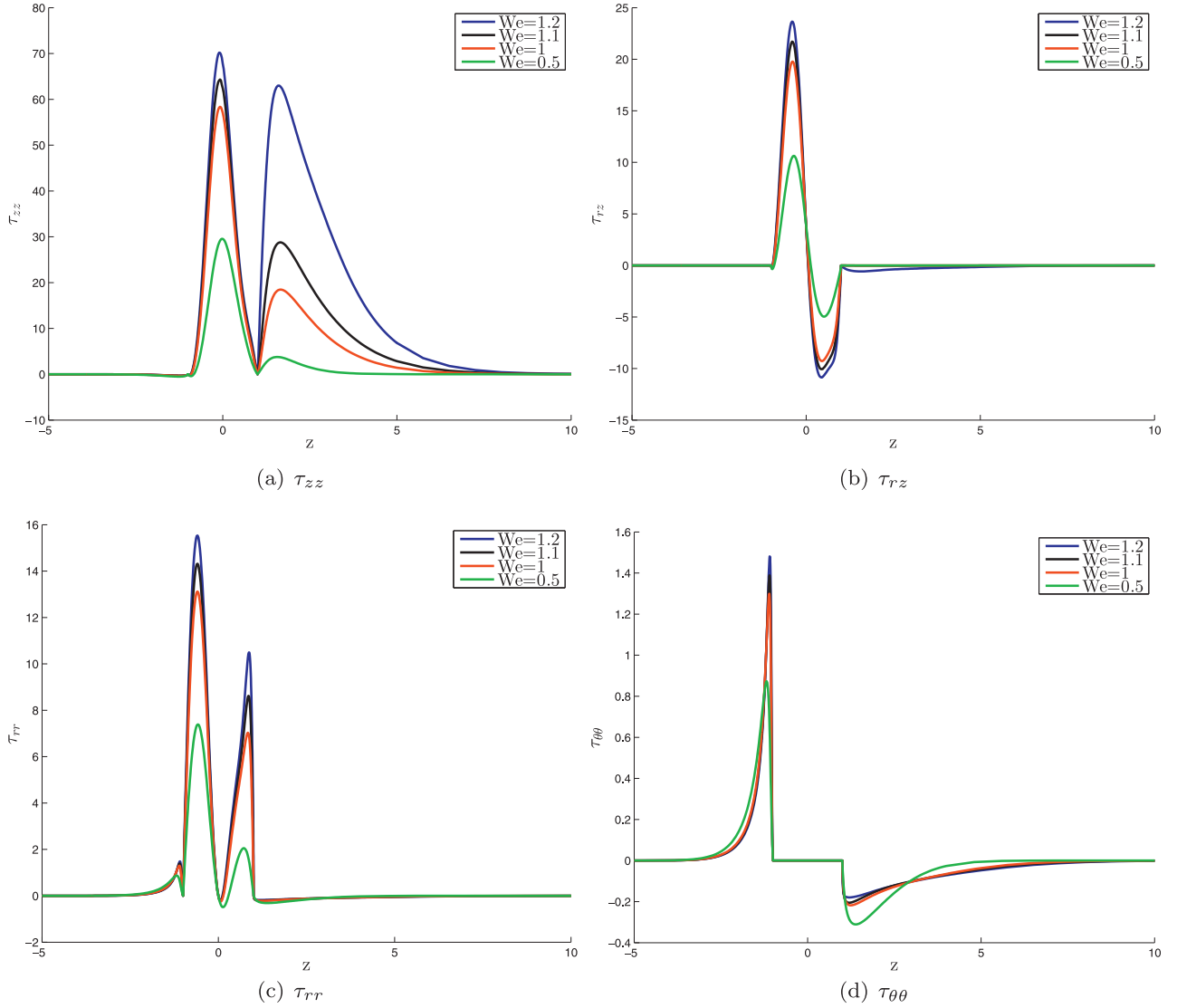
5.2. Flow past a fixed sphere

We now consider the benchmark problem of flow past a fixed sphere as described in Section 3 with $Re = 0.01$ and consider $\beta = \frac{1}{9}$ and $\beta = \frac{1}{2}$ and increase We in increments of 0.1 until we can no longer compute a solution. Calculations are performed on

meshes M1–M4, (see Fig. 4). Mesh M1 is a symmetric mesh fore and aft of the sphere comprising 26 elements while M2 features additional refinement in the wake of the sphere along the axis of symmetry. Meshes M3 and M4, which derive from mesh M2, are used for computations at values of We near the maximum attainable value and feature additional refinement radially outwards from the sphere and in the wake. We fix $\Delta t = 10^{-4}$ and perform refinement with N for each of these meshes. Note that the geometry is represented precisely for all meshes through an exact parametrisation the circular boundary.

The numerical algorithm is terminated when $S^n < \epsilon$ where

$$S^n = \frac{1}{\Delta t} \sqrt{ \frac{\|p^n - p^{n-1}\|^2_{L^2(\Omega)} + \|\mathbf{u}^n - \mathbf{u}^{n-1}\|^2_{H^1(\Omega)} + \|\boldsymbol{\tau}^n - \boldsymbol{\tau}^{n-1}\|^2_{L^2(\Omega)}}{\|p^n\|^2_{L^2(\Omega)} + \|\mathbf{u}^n\|^2_{H^1(\Omega)} + \|\boldsymbol{\tau}^n\|^2_{L^2(\Omega)}} } \tag{54}$$

Fig. 10. Components of elastic stress along the axis of symmetry for uniform flow of an Oldroyd B fluid past a fixed sphere in a cylinder. Model parameters $\beta = 0.5$, $Re = 0.01$.

and ϵ is a threshold value, typically 10^{-7}, or when a set time limit of 40 is reached, i.e. $n\Delta t > 40$. In the case where the time limit is reached we will treat the final timestep as the steady state result, but will mark values obtained from such simulations with an asterisk in our tables of results.

The drag on the sphere is given by

$$D = 2\pi R_S^2 \int_0^\pi \left(\left(p - 2\beta \nabla \mathbf{u}_{zz} - \tau_{zz} \right) \cos \theta \right.$$

$$\left. + \left(\beta (\nabla \mathbf{u}_{rz} + \nabla \mathbf{u}_{zr}) + \tau_{rz} \right) \sin \theta \right) \sin \theta \, d\theta. \quad (55)$$

and the drag factor is calculated using (1) in order to draw comparison with other results in the literature. As an initial validation exercise we calculated the drag factor for steady-state Stokes flow past a sphere and obtained a converged value of 5.9474, which is in agreement with results in the literature [9,34,35].

5.2.1. Oldroyd B

We begin by examining the drag results for the Oldroyd B model. Performing refinement with respect to N on mesh M1 we reach a maximum attainable Weissenberg number of $We = 0.7$ for $\beta = 0.5$, with results shown in Table 2. Note that the result

for $We = 0.7$ at $N = 15$ failed to meet the tolerance set on the stopping criterion in Eq. (54) within the prescribed time limit. This means that the velocity, pressure or stress fields had not converged to steady state, although the computation had not diverged. In this case it is clear that the stress field had not reached a steady state. Increasing N resolves this problem for this value of We. However, we are unable to reach higher We for all simulations despite further p-refinement.

In Table 3 the drag factor is presented using similar refinement on mesh M2 and are able to achieve results up to $We = 1.2$. A steady state result which met our stopping criterion was not attained for $We > 1$. The additional refinement in the wake allows the method to reach a higher attainable We compared to mesh M1. This agrees well with other findings in the literature where additional refinement in the wake of the sphere was also found to be necessary in order to increase the maximum attainable We. Table 4 presents the drag factor on M2 for $\beta = \frac{1}{9}$. We obtain steady state results which meet the stopping criterion for $0 \leq We \leq 0.9$. For $We > 0.9$, a steady state approximation was not obtained.

Despite not reaching a steady state according to our stopping criterion, these results appear positive. However, near the maximum attainable We, the drag is slowly diverging with time. Focus-
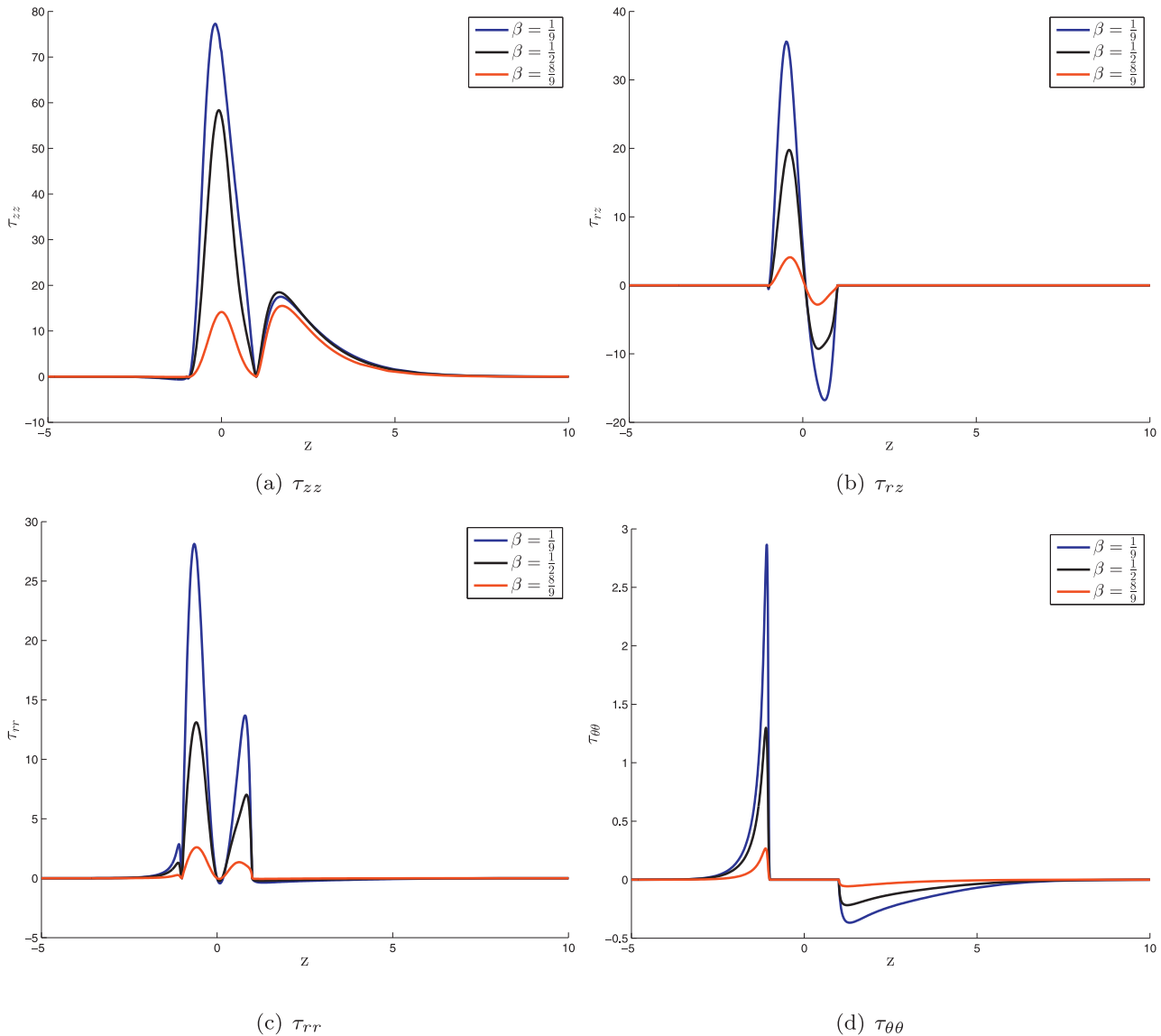
(a) τ_{zz}

(b) τ_{rz}

(c) τ_{rr}

(d) $\tau_{\theta\theta}$

Fig. 11. Components of elastic stress along the axis of symmetry for uniform flow of an Oldroyd B fluid past a fixed sphere in a cylinder. Model parameters $We = 1$, $Re = 0.01$.

Table 8
Comparison of number of degrees of freedom. An estimate of the degrees of freedom used for each field variable is included.

K	N	$\mathbf{u}$	p	$\boldsymbol{\tau}$	$\mathbf{G}$	Total
31	12	8712	3751	17424	18755	48642
31	16	15584	6975	31168	34875	88602
52	16	26176	11700	52352	58500	148728
Bodart & Crochet		~7000	~1000	~55000	–	62623
Chauvière & Owens, $N = 8$.		13314	4900	26628	–	44842
Adaptive SUPG-EE.		~8000	~2400	~16000	–	26273
Lunsmann et al.		~17000	~1500	~34000	–	51354

ing on $\beta = \frac{1}{2}$, Fig. 5(a) shows that the computed drag oscillates with increasing amplitude at $We = 1.1$ and 1.2 away from a steady value in time, with the increase in amplitude at $We = 1.2$ being most pronounced as can be seen clearly in Fig. 5(b) where the deviation of the drag factor from the approximate centre of oscillation is shown. Furthermore, as shown in Fig. 5(c) and (d), the amplitude of the oscillations increases with increasing N due to the inability to resolve the stress in the wake or the thin stress boundary layer on the sphere nearest the cylindrical wall. This is con-

firmed by examining the components of elastic stress which contribute to the drag, shown in Fig. 6, at the final timestep of the simulation, for $We = 1.1$ and 1.2. This shows that the dominant source of the numerical breakdown near the surface of the sphere, most likely due to the inability to resolve the thin boundary layer that develops.

To investigate if this can be resolved with further mesh refinement, the simulations are repeated on meshes M3 and M4. At fixed N and relative to mesh M2, mesh M3 increases the number of
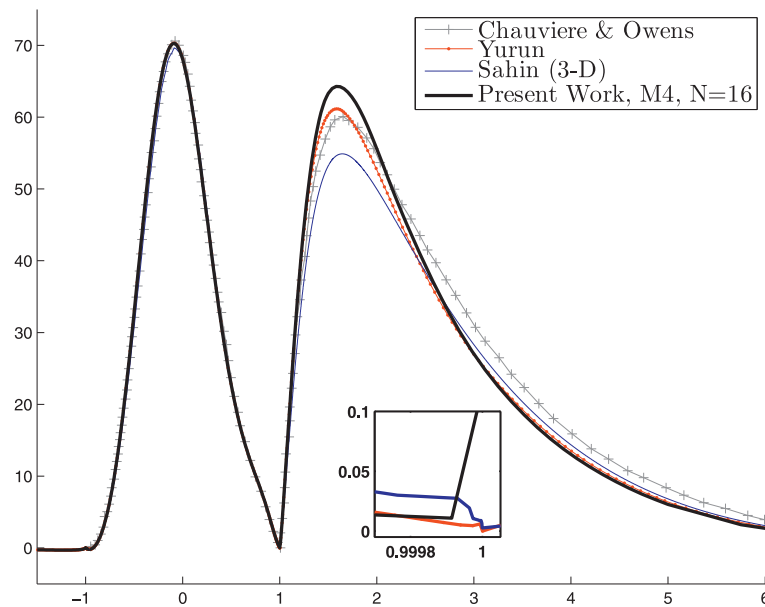
Fig. 12. Comparison of τ_{zz} at $We = 1.2$, $\beta = \frac{1}{2}$ with results in the literature.

degrees of freedom normal to the sphere surface. Mesh M4 increases the number of degrees of freedom tangent to the sphere surface. Table 5 shows the results at values of We leading to 1.3. We fail to reach a steady state according to our stopping criterion for all values of N above $We = 1$ and are unable to reach $We = 1.3$. The value of the drag we compute is only subtly different from that computed on mesh M2. However on Mesh $M4$, as Fig. 7(a) shows, the drag is no longer diverging over time at $We \leq 1.2$. While the simulation broke down at $We = 1.3$, we find that the drag is oscillating around a value of 5.1765 before diverging. As can be seen from Fig. 7(b), the deviation of the drag over time on mesh M3 shows very little improvement over mesh M2 and we do not see any apparent benefit from its use over mesh M2 in terms of progressing the simulations in time or in the resolution of the stress in the boundary layer at the top of the sphere nearest the cylindrical wall.

Mesh M4, however, yields a reduction in the oscillations in the drag factor and yields some notable improvements, suggesting that we had lacked sufficient resolution tangent to the sphere's surface. Further, Fig. 7(c) and (d) show that increasing N no longer leads to an increase in the amplitude of the oscillations. Note that the axis range is fixed for the $We = 1.1$ and $We = 1.2$ plots to allow a direct comparison. We no longer see the dramatic increase in the amplitude of the oscillations when increasing We from 1.1 to 1.2 as with mesh M2. The amplitude of the oscillation for $We = 1.1$ is reducing over time and the drag appears to be converging, suggesting that the simulation would remain stable over a larger time limit. At $We = 1.2$, increasing N leads to a reduction in the amplitude of the oscillations but with the varying amplitude it is not so clear that the simulation would remain stable with an increased time limit. However, the improvement over the other meshes is clear, highlighting the importance of spatial refinement in the appropriate manner even with high-order methods.

Fig. 8 presents profiles of the components of the elastic stress which contribute to the drag at $We = 1.1$ and $We = 1.2$ computed on mesh M4 for increasing N at the final timestep of the simulation. Note that, unlike on the surface of the sphere, the stress components in the wake are not fully resolved on this or any of our meshes and convergence with N has not been attained.

Results obtained on mesh M4 are used to make comparisons with the literature in Tables 6 and 7 and Fig. 9. Excellent agree-

Table 9

Drag factor for flow past a fixed sphere in a cylinder for a Giesekus fluid at $Re = 0.01$. Performed with timestep, $\Delta t = 10^{-4}$ using DEVSS-G, $\beta_s = 1$. Collected from Tables of results within Section 5.2.2.

	$\beta = \frac{1}{9}$			$\beta = \frac{1}{2}$		
We	$\alpha = 0.001$	$\alpha = 0.01$	$\alpha = 0.1$	$\alpha = 0.001$	$\alpha = 0.01$	$\alpha = 0.1$
0.1	5.85454	5.71976	5.20328	5.89599	5.82188	5.60472
0.2	5.66254	5.43594	4.58572	5.79023	5.66614	5.24331
0.3	5.44242	5.16094	4.20120	5.67023	5.51530	5.02777
0.4	5.23256	4.91556	3.91824	5.55706	5.38097	4.86667
0.5	5.04752	4.70415	3.69245	5.45841	5.26557	4.73752
0.6	4.89028	4.52447	3.50490	5.37568	5.16781	4.63034
0.7	4.75903	4.37213	3.34538	5.30777	5.08520	4.53948
0.8	4.65044	4.24254	3.20757	5.25277	5.01511	4.46132
0.9	4.56096	4.13154	3.08716	5.20863	4.95519	4.39332
1	4.48740*	4.03564	2.98105	5.17347	4.90346	4.33360
1.1	4.42836*	3.95202*	2.88688	5.14568*	4.85834	4.28074
1.2	–	–	2.80282	5.12387*	4.81854	4.23365
1.3	–	–	2.72738*	–	4.78314	4.19142
1.4	–	–	2.65936*	–	4.75133*	4.15336
1.5	–	–	–	–	4.72258*	4.11888
1.6	–	–	–	–	–	4.08750
1.7	–	–	–	–	–	4.05881
1.8	–	–	–	–	–	4.03250
1.9	–	–	–	–	–	4.00827
2	–	–	–	–	–	3.98588

ment for the drag factor is found with Chauvière and Owens [5] for $\beta = 0.5$ and Bodart and Crochet [10] for $\beta = \frac{1}{9}$. The limiting value of We for both $\beta = \frac{1}{9}$ and $\beta = \frac{1}{2}$ lies between 1.2 and 1.3. This agrees with the findings in these papers.

Plots of the stress along the axis of symmetry and surface of the sphere are shown in Fig. 10 for $\beta = 0.5$ as a function of We and in Fig. 11 for $We = 1$ as a function of β. A sharp increase in the axial stress on the surface and in the wake of the sphere and in the radial stress on the surface of the sphere is found as We increases. Additionally, the overshoot in the axial stress extends further downstream as We increases, particularly from 1.1 to 1.2. This suggests that the breakdown in simulations after $We = 1.2$ is most likely due to the inability of the approximation to capture the stress gradients around the sphere and in the wake region. Both Yurun [12] and Chauvière and Owens [5] suggest that there is a physical instability near $We = 1.3$ at $\beta = 0.5$ (Yurun suggests
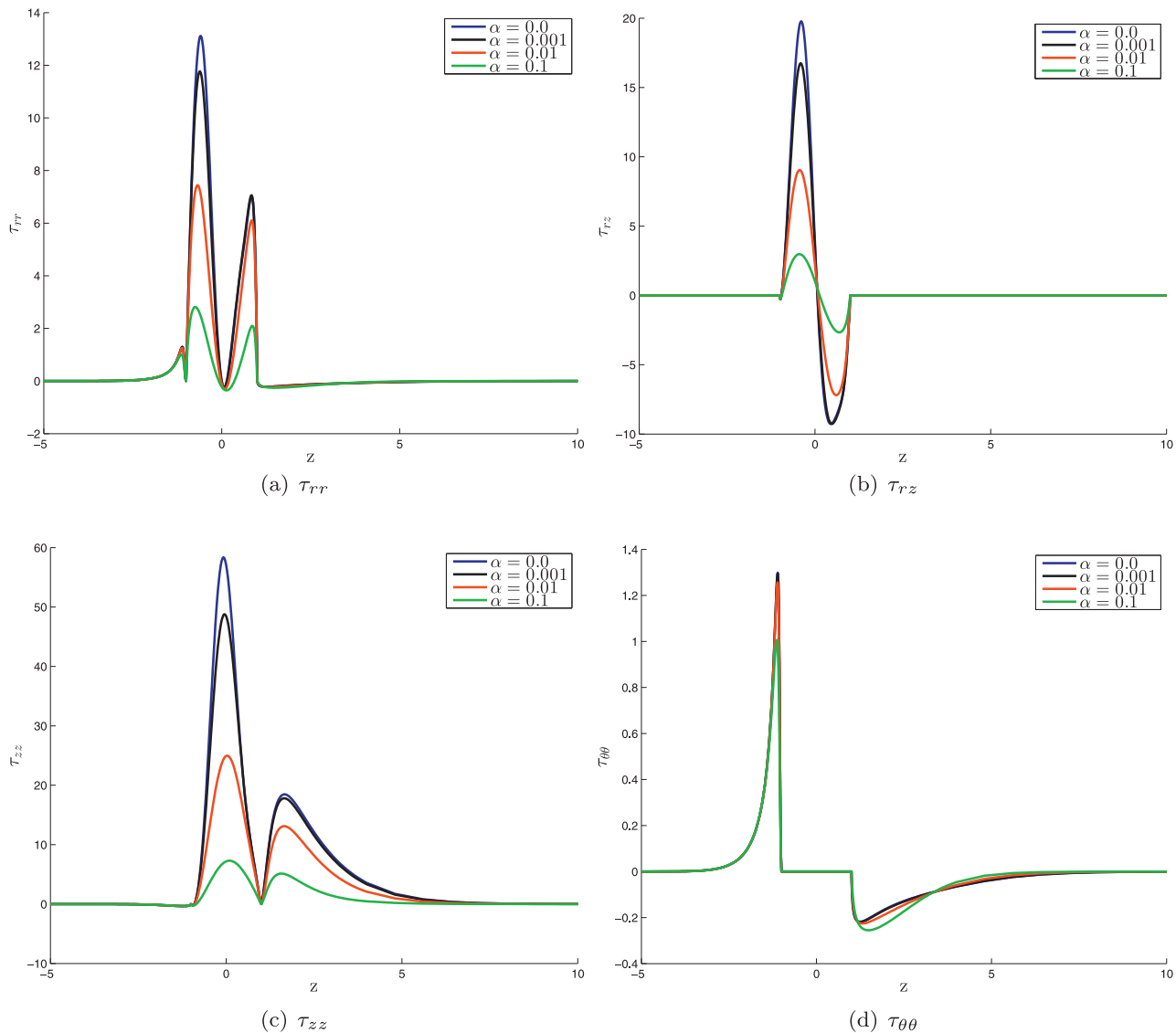
Fig. 13. Components of elastic stress along the axis of symmetry for Giesekus fluid flow past a fixed sphere in a cylinder. Model parameters $\beta = 0.5$, $Re = 0.01$ and $We = 1$. Numerical parameters, $\Delta t = 10^{-4}$, $N = 16$ on mesh M2 using DEVSS-G with $\beta_s = 1$.

it lies somewhere between 1.26 and 1.3) for the Oldroyd B model - our results seem to support this. With decreasing β we see that while the axial stress on the surface of the sphere is further enhanced, the change in the wake of the sphere is minimal, which explains why our simulations produce very similar maximum achievable We and if sufficient mesh refinement is used to resolve the boundary layer on the surface of the sphere, it is the stress in the wake near the rear stagnation point which is the limiting factor for our computations. As Yurun [12] points out, this is where the fluid undergoes a sudden change from shearing to extensional behaviour.

A comparison of τ_{zz} with several results in the literature [5,12,36] for $We = 1.2$, $\beta = 0.5$ is shown in Fig. 12. Very good agreement is obtained along the surface of the sphere, but there is a lack of close agreement in this component of stress in the wake. Note that the present method captures a very sharp gradient at the rear stagnation point (see the inset in Fig. 12).

Table 8 provides a comparison of the numbers of degrees of freedom required by the method described in this paper with those of Bodart and Crochet [10], Lunsmann et al. [9] and Chauvière and Owens [5]. It should be noted that while the total

number of degrees of freedom for the method described in this paper appears to be high, the unknowns associated with the stress and velocity gradient tensors are decoupled from the velocity and pressure unknowns and are not determined through the solution of the global linear system. This means that only the degrees of freedom associated with velocity and pressure make a substantial contribution to the computational effort required.

As with the other authors, convergence of the axial stress in the wake with mesh or polynomial refinement for $We = 1.2$ has not been demonstrated at present. The lack of convergence may be due to a number of reasons including an inability to resolve steep gradients due to the substantial additional computational resources required or the breakdown of the axisymmetric assumption for a value of We in this range. Sahin [37] found three-dimensional instabilities in the wake for the flow of an Oldroyd-B fluid past a confined cylinder. This has been confirmed by Damanik et al. [38].

Any further attempts to resolve the stress gradients would require additional refinement using a combination of adaptive h-refinement, using of hanging nodes, and adaptive p-refinement on an element-by-element basis. This would allow very high-order ($N > 16$) spectral elements to be used in regions that require
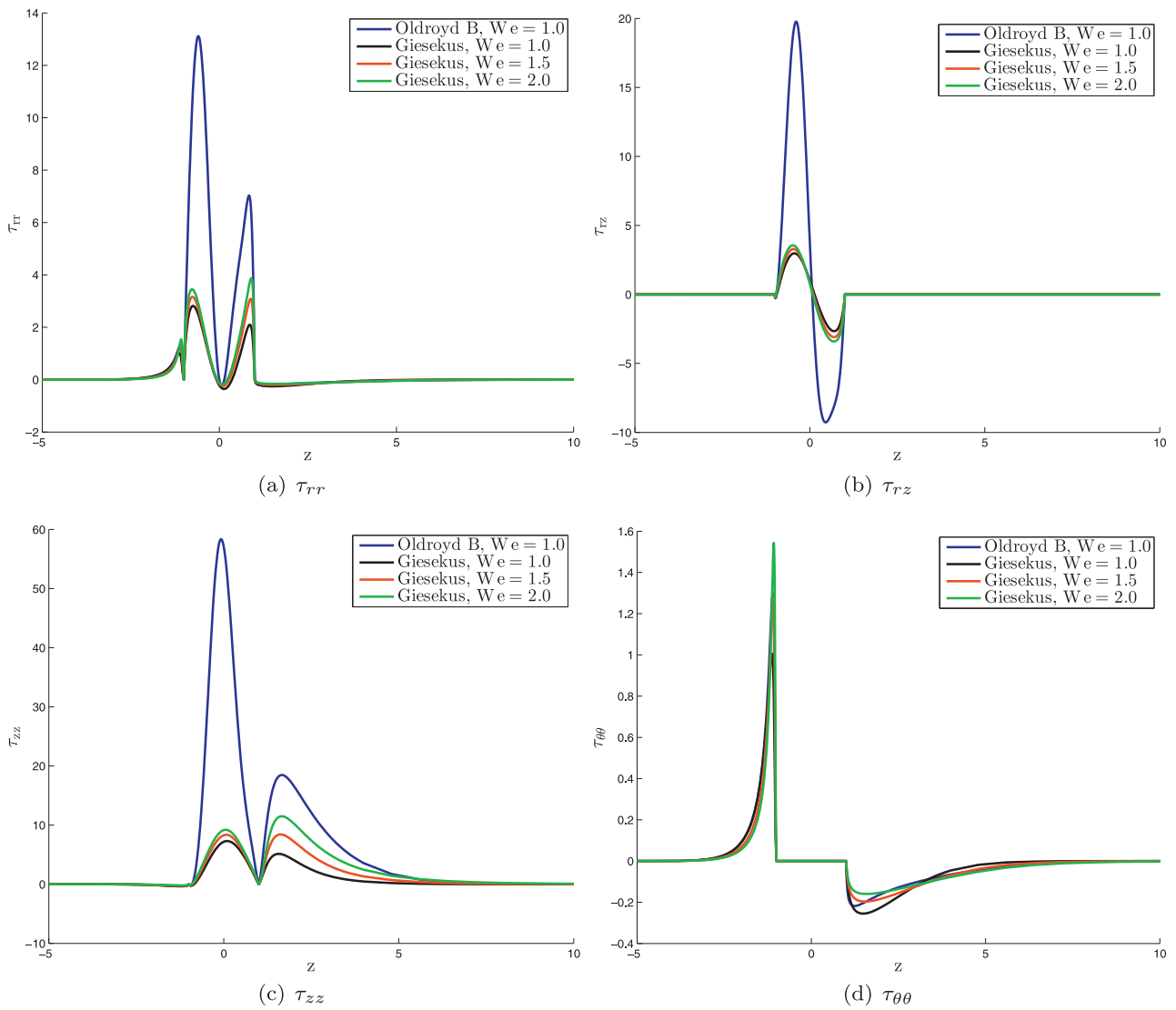
Fig. 14. Components of elastic stress along the axis of symmetry for Giesekus fluid flow past a fixed sphere in a cylinder. Model parameters $\beta = 0.5$, $Re = 0.01$ and $\alpha = 0.1$. Numerical parameters, $\Delta t = 10^{-4}$, $N = 16$ on mesh M2 using DEVSS-G with $\beta_s = 1$.

steep gradients to be resolved and low-order spectral elements elsewhere.

5.2.2. Giesekus

In this section we present results for the Giesekus model in order to provide benchmark results for others to use as a basis for comparison and also to investigate the influence of the mobility parameter on the drag. We consider values of the mobility parameter $\alpha = 0.001$, 0.01 and 0.1. Table 9 presents the drag factor for $0 \leq We \leq 2$. There is a clear decrease in the drag factor at equivalent We and β values when compared to the Oldroyd B model. The drag reduction can be explained by the shear thinning behaviour of the Giesekus model. This reduces the strength of the stress boundary layer on the surface of the sphere nearest the wall and accounts for the decrease in drag in comparison to the Oldroyd B model.

At $\beta = \frac{1}{2}$, an increase in the mobility parameter results in a far higher attainable Weissenberg number than the Oldroyd B model. In fact we could attain converged results for $We > 2$ when $\alpha = 0.1$. However, for $\beta = \frac{1}{9}$, the attainable Weissenberg number is only marginally higher at 1.4 compared to 1.1. This may at first appear strange, as the behaviour in the wake of the sphere is reduced by the extensional behaviour of the Giesekus model, and yet the

simulation still breaks down. One possible explanation is that the extensional viscosity, while remaining finite, experiences a high rate of increase in the transition (under increasing elongation rate) to the limiting value. The rate of increase of the extensional viscosity decreases with increasing α and β, allowing the simulations at $\alpha = 0.1$ and $\beta = 0.5$ to converge at higher values of We.

Fig. 13 presents plots of the elastic stress components along the axis of symmetry and surface of the sphere at $We = 1$ and $\beta = 0.5$ with increasing α. Here we see the effect of the decreased extensional viscosity in the reduction of the axial stress in the wake of the sphere. The reduction in the axial stress from the Oldroyd B model to Giesekus with $\alpha = 0.001$ is minimal in the wake. It is more pronounced at $\alpha = 0.01$ and very prominent at $\alpha = 0.1$. This supports the suggestion above that the behaviour of the axial stress, resulting from extensional properties of the model, enables higher Weissenberg numbers to be attained.

Fig. 14 presents the same plots as above but this time for $\beta = 0.5$, $\alpha = 0.1$ and increasing We. This highlights the role of the Weissenberg number in the growth of the axial stress in the wake of the sphere. At $We = 2$ the maximum axial stress is approximately half that for the Oldroyd B value at $We = 1$

where simulations begin to break down. We speculate that further increasing of *We* with these values of α and β will lead to an increase in the axial stress until the stress gradients are too sharp to be captured by polynomial refinement and the simulation will break down, similar to the others.

6. Conclusions

We have presented a DG/DEVSS-G spectral element method for axisymmetric viscoelastic flows and presented a comprehensive set of results on the benchmark problem of flow past a sphere. This axisymmetric problem is solved numerically and convergence is demonstrated with respect to polynomial order. Increased *h*-type convergence is also considered by increasing the number of elements. The method allows high resolution modelling of viscoelastic flows and the numerical approximation of the drag factor that agree closely with the available results in the literature. We have also considered the Giesekus model for a range of mobility parameter values and present them with the intention that other researchers may validate against and make comparison with our results.

For the Oldroyd B model we have found excellent agreement with the results available in the literature for the drag experienced by the sphere. We have found that a combination of polynomial enrichment and mesh refinement is required to attain results for Weissenberg numbers greater than 1 and that, above this value, the drag becomes increasingly oscillatory due to the difficulty in capturing the stress at a steady state. The high resolution of the spectral element method allows for detailed investigation of the behaviour of the stress fields in the wake of the sphere and provides additional evidence that the numerical breakdown is, in part, caused by an inability to capture the high gradients in the axial stress present in this region of elongational flow. It is reasonable to suspect that the unphysical behaviour of the Oldroyd B model may be the root of the problem. However, the problem may also be related to the axisymmetric flow assumption since three-dimensional simulations for the Oldroyd-B fluid past a confined cylinder indicates three-dimensional instabilities in the viscoelastic wakes [37,38].

For the Giesekus model, we find that there is a reduction in drag experienced by the sphere when compared to the Oldroyd B model at equivalent *We* and β. This is explained by the shear thinning properties of the model. Additionally, we have found that an increase in the mobility parameter leads to higher attainable Weissenberg numbers, but a breakdown in the numerical simulation is still present at $We < 2$ for $\alpha < 0.1$. This suggests that the infinite extensional viscosity behaviour of the Oldroyd B model is not the sole cause of numerical breakdown and that other factors must be considered. For example, the fixed-point iteration for updating the stress (see (23)) is not a fully implicit treatment of these terms in time and so this may be a source of numerical instability. We have found that the high gradients in the axial stress are still present in the wake of the sphere and that growth with increasing *We* is delayed by increasing the mobility parameter. Ultimately, it appears that numerical breakdown with increasing *We* for methods using polynomial basis functions in this benchmark problem is inevitable for the Giesekus model despite the favourable extensional properties.

Acknowledgements

References

[1] O. Hassager, Working group on numerical techniques, J. Non-Newtonian Fluid Mech. 29 (1988) 2–5.

[2] G.G. Stokes, On the theories of the internal friction of fluids in motion, and of the equilibrium and motion of elastic solids., Trans. Camb. Phil. Soc. 8 (1845) 287–305.

[3] E.R. Lindgren, The motion of a sphere in an incompressible viscous fluid at Reynolds numbers considerably less than one, Physica Scripta 60 (2) (1999) 97.

[4] R.G. Owens, T.N. Phillips, Computational Rheology, Imperial College Press, 2002.

[5] C. Chauvière, R.G. Owens, How accurate is your solution?: error indicators for viscoelastic flow calculations, J. Non-Newtonian Fluid Mech. 95 (1) (2000) 1–33.

[6] H.K. Rasmussen, O. Hassager, Simulation of transient viscoelastic flow, J. Non-Newtonian Fluid Mech. 46 (1993) 289–305.

[7] M.J. Crochet, V. Legat, The consistent streamline-upwind/Petrov-Galerkin method for viscoelastic flow revisited, J. Non-Newtonian Fluid Mech. 42 (1992) 283–299.

[8] F.P.T. Baaijens, S.H.A. Selen, H.P.W. Baaijens, G.W.M. Peters, H.E.H. Meijer, Viscoelastic flow past a confined cylinder of a low density polyethylene melt, J. Non-Newtonian Fluid Mech. 68 (2) (1997) 173–203.

[9] W.J. Lunsmann, L. Genieser, R.C. Armstrong, R.A. Brown, Finite element analysis of steady viscoelastic flow around a sphere in a tube: calculations with constant viscosity models, J. Non-Newtonian Fluid Mech. 48 (1993) 63–99.

[10] C. Bodart, M.J. Crochet, The time-dependent flow of a viscoelastic fluid around a sphere, J. Non-Newtonian Fluid Mech. 54 (1994) 303–329.

[11] H.R. Tamaddon-Jahromi, M.F. Webster, P.R. Williams, Excess pressure drop and drag calculations for strain-hardening fluids with mild shear-thinning: contraction and falling sphere problems, J. Non-Newtonian Fluid Mech. 166 (16) (2011) 939–950.

[12] Y. Fan, Limiting behavior of the solutions of a falling sphere in a tube filled with viscoelastic fluids, J. Non-Newtonian Fluid Mech. 110 (2–3) (2003) 77–102.

[13] B. Yang, B. Khomami, Simulations of sedimentation of a sphere in a viscoelastic fluid using molecular based constitutive models, J. Non-Newtonian Fluid Mech. 82 (2) (1999) 429–452.

[14] O.G. Harlen, The negative wake behind a sphere sedimenting through a viscoelastic fluid, J. Non-Newtonian Fluid Mech. 108 (1) (2002) 411–430.

[15] S. Claus, T.N. Phillips, Viscoelastic flow around a confined cylinder using spectral/hp element methods, J. Non-Newtonian Fluid Mech. 200 (2013) 131–146.

[16] D. Rh. Gwynllyw, T.N. Phillips, On the enforcement of the zero mean pressure condition in the spectral element approximation of the Stokes problem, Comp. Methods App. Mech. Eng. 195 (2006) 1027–1049.

[17] H. Giesekus, A simple constitutive equation for polymer fluids based on the concept of deformation-dependent tensorial mobility, J. Non-Newtonian Fluid Mech. 11 (1982) 69–109.

[18] J.G. Oldroyd, On the formulation of rheological equations of state, Proc. R. Soc. Lond. A 200 (1950) 523–541.

[19] M. Renardy, Mathematical Analysis of Viscoelastic Flows, SIAM, Philadelphi, 2000.

[20] A.W. Liu, D.E. Bornside, R.C. Armstrong, R.A. Brown, Viscoelastic flow of polymer solutions around a periodic, linear array of cylinders: comparisons of predictions for microstructure and flow fields, J. Non-Newtonian Fluid Mech. 77 (3) (1998) 153–190.

[21] A.C.B. Bogaerds, A.M. Grillet, G.W.M. Peters, F. Baaijens, Stability analysis of polymer shear flows using the extended pom–pom constitutive equations, J. Non-Newtonian Fluid Mech. 108 (1) (2002) 187–208.

[22] Y. Maday, A.T. Patera, M. Rønquist, An operator-integration-factor splitting method for time-dependent problems: application to incompressible fluid flow, J. Sci. Comp. 5 (4) (1990) 263–292.

[23] G.E. Karniadakis, M. Israeli, S.A. Orszag, High-order splitting methods for the incompressible Navier-Stokes equations, J. Comput. Phys. 97 (2) (1991) 414–443.

[24] W.J. Gordon, C.A. Hall, Transfinite element methods: blending function interpolation over arbitrary curved element domains, Numer. Math. 21 (1973) 109–129.

[25] C. Schneidesch, M.O. Deville, Chebyshev collocation method and multi-domain decomposition for Navier-Stokes equations in complex curved geometries, J. Comput. Phys. 105 (1993) 234–257.

[26] F. Belblidia, H. Matallah, M. Webster, Alternative subcell discretisations for viscoelastic flow: velocity-gradient approximation, J. Non-Newtonian Fluid Mech. 151 (1) (2008) 69–88.

[27] P. Lesaint, P.A. Raviart, On AFinite Element Method for Solving the Neutron Transport Equation, Univ. Paris VI, Labo. Analyse Numérique, 1974.

[28] M. Fortin, A. Fortin, A new approach for the FEM simulation of viscoelastic flows, J. Non-Newtonian Fluid Mech. 32 (3) (1989) 295–310.

[29] O. Schenk, K. Gärtner, Solving unsymmetric sparse systems of linear equations with PARDISO, Future Gener. Comput. Syst. 20 (3) (2004) 475–487.

[30] N.D. Waters, M.J. King, Unsteady flow of an elastico-viscous liquid in a straight pipe of circular cross section, J. Phys. D 4 (1971) 204–211.

[31] S. Xu, A.R. Davies, T.N. Phillips, Pseudospectral method for transient vis-coelastic flow in an axisymmetric channel, Numer. Methods PDE 9 (6) (1993) 691–710.

[32] M.E. Ryan, A. Dutta, Analysis of the constant rate startup flow of a viscoelas-tic fluid in annular, cylindrical, and planar conduits, J. Rheol. 25 (2) (1981) 193–212.

[33] R.G.M. van Os, T.N. Phillips, The prediction of complex flows of polymer melts using spectral elements, J. Non-Newtonian Fluid Mech. 122 (2004) 287–301.

[34] R.O. Vargas, O. Manero, T.N. Phillips, Viscoelastic flow past confined objects using a micro-macro approach, Rheol. Acta 49 (2009) 373–395.

[35] R.G. Owens, T.N. Phillips, Steady viscoelastic flow past a sphere using spectral elements, Int. J. Numer. Methods Eng. 39 (1996) 1517–1534.

[36] E. Oner, M. Sahin, A parallel adaptive viscoelastic flow solver with template based dynamic mesh refinement, J. Non-Newtonian Fluid Mech. 234 (2016) 36–50.

[37] M. Sahin, Parallel large-scale numerical simulations of purely-elastic instabili-ties behind a confined circular cylinder in a rectangular channel, J. Non-New-tonian Fluid Mech. 195 (14) (2013) 46–56.

[38] H. Damanik, O. Mierka, A. Ouazzi, S. Turek, A multigrid LCR–FEM solver for vis-coelastic fluids with application to problems with free surface, 2013Enumath.